

1

2 **INFLUENCE OF MHD WAVES ON DIFFUSE REGIONS OF**
3 **MOLECULAR CLOUDS AND MAGNETICALLY ALIGNED**
4 **STRIATIONS**

5

by

6

Rahul Khanna

7

Graduate Program in Astronomy

8

A thesis submitted in partial fulfillment
of the requirements for the degree of
Masters of Science

9

10

11

The School of Graduate and Postdoctoral Studies
The University of Western Ontario
London, Ontario, Canada

12

13

14

© Rahul Khanna 2025

¹⁵

THE UNIVERSITY OF WESTERN ONTARIO
School of Graduate and Postdoctoral Studies

¹⁶

¹⁷

Thesis Title:

¹⁸

Influence of MHD Waves on diffuse regions of molecular clouds and
magnetically aligned striations

¹⁹

²⁰

Author: Rahul Khanna

²¹

Program: Astronomy

²²

Master of Science

²³

Astronomy (Scientific Computing)

²⁴

September 2024 - December 2025

²⁵

Supervisor: Prof. Shantanu Basu

²⁶

Advisory Committee: Prof. Eugene Wong and Prof. Mark Baker

Acknowledgements

28 First and foremost, I would like to express my sincere gratitude and appre-
29 ciation to my mentor, guide and supervisor Prof. Shantanu Basu. His sup-
30 port, guidance and mentorship were the backbone of the academic and research
31 progress I achieved. Without his invaluable insights, essential advices and con-
32 stant encouragement and motivation, the completion of this project would not
33 have been possible. Throughout this journey, he has been my inspiration and I
34 have learned a lot from him both academically and personally.

35

36 I also want to thank Prof. Shahram Abbassi under whom I worked and fin-
37 ished another amazing project, which is now submitted. His guidance and
38 mentorship has kept me motivated and focused. I want to appreciate the help
39 and support of my friends: Majd, Pratik, Nishtha, Dilanjan and Arsh. Having
40 scientific and life-related discussions with them made this journey smooth, in-
41 teresting and much more enjoyable.

42

43 Finally, I want to thank my Mom, Dad and my sister Shefali for their con-
44 stant support, love and care. Words cannot describe how much I appreciate the
45 strength and confidence they have given me over the years. This journey would
46 not have been possible without all their efforts, love and support.

Abstract

The influence of magnetohydrodynamic (MHD) waves on molecular clouds and the interstellar medium is becoming an active area of research. Recently, numerical studies and observations have found that the outer low-density regions of molecular clouds are shaped by MHD waves. Thread-like quasi-periodic structures called striations have been observed in these regions, and studies have suggested they are the imprints of compressive MHD waves. We perform 2D ideal MHD simulations using ATHENA++ to examine: (i) the evolution and influence of transverse and longitudinal MHD waves on low-density regions and (ii) the role of MHD waves in defining the formation and growth of striations on different scales. In our models, we introduce a source of MHD perturbations influxed into a low-density medium. We also introduce a constant gravitational field in two of our models to understand the influence of density stratification. We find that under constant gravity and stratified density conditions, striations form and evolve with density contrasts and periodicities similar to observations. Density and velocity power spectra at different times provide evidence that compressive MHD waves are trapped and that their power redistributes to lower spatial frequencies, resembling the structure and the formation timescales of striations observed at large scales. Our findings suggest that the strength of the magnetic field plays an important role in the dynamics and structural shift seen in diffuse molecular clouds. For a range of magnetic field strengths (v_A/c_s between 2 and 4), we find excellent agreement between the simulation results and observations. We conclude that small-scale striations may hint at weak magnetic field strengths or early formation stages, whereas large-scale striations take longer to form and require stronger background magnetic field strengths.

Keywords: Interstellar medium —Interstellar Magnetic Fields — Molecular Clouds—
Magnetohydrodynamics — Gravitational Field — MHD simulations

Contents

71

72	Acknowledgements	iii
73	Abstract	iv
74	1 Introduction	1
75	2 Background	7
76	3 Method	9
77	3.1 Simulation Setup	9
78	3.2 Initial Conditions	9
79	3.3 New Boundary Conditions	11
80	4 Results	13
81	4.1 Uniform Density Field	13
82	4.2 Stratified field under low gravity	16
83	4.3 Stratified field under high gravity	20
84	4.4 Influence of MHD waves	22
85	4.5 Evolution of MHD waves	27
86	5 Discussion	33
87	6 Conclusion	38
88	7 Future Work	40
89	Appendix	46
90	A Fast magnetosonic equation	47
91	B Convergence Test	49
92	C Magnetic Field Calculations	51

⁹³ Chapter 1

⁹⁴ Introduction

⁹⁵ Magnetic fields have been observed throughout the universe across all scales. Starting with
⁹⁶ Earth's own magnetic field that protects us from harmful solar and cosmic radiation, researchers
⁹⁷ have also found magnetic field(s) surrounding our sun, preserved inside the interstellar medium,
⁹⁸ mainly molecular clouds present between the stars and at galactic scales. Our own galaxy, the
⁹⁹ Milky Way, has a large-scale magnetic field with a strength estimated at a few μG . These mag-
¹⁰⁰ netic fields are maintained by the presence of electrons and an ionic plasma, which generates
¹⁰¹ charged currents. In some regions, gravity or turbulence is dynamically more important than
¹⁰² magnetic fields, and magnetic fields are largely ignored. However, in several important areas
¹⁰³ of astrophysics, magnetic fields are dynamically important, including star formation, accretion
¹⁰⁴ disks, supermassive black holes (SMBHs), neutron stars, interstellar and intergalactic medium
¹⁰⁵ and many more. This makes the magnetic field a crucial physical aspect of most astrophysical
¹⁰⁶ systems and requires more exploration across theoretical, numerical and observational avenues.
¹⁰⁷

¹⁰⁸ In recent years, interest in exploring and understanding magnetic fields has grown. Our un-
¹⁰⁹ derstanding of how large-scale magnetic fields are preserved and the dynamical impact on their
¹¹⁰ host regions is still relatively new, and many avenues remain to be explored. The first challenge
¹¹¹ we face when dealing with magnetic fields is measuring them precisely. Some methodologies
¹¹² and instrumentation have been proposed and applied to estimate magnetic field strengths; how-
¹¹³ ever, precise calculations remain difficult. Although we can precisely evaluate the orientation
¹¹⁴ of large-scale magnetic fields from dust polarization observations. These results measure ori-
¹¹⁵ entation along the plane-of-sky, and there remains a lack of advanced methods that can estimate
¹¹⁶ the line-of-sky components. Secondly, their dynamical influence remains poorly understood.
¹¹⁷ Many researchers use a state-of-the-art high-resolution numerical simulation approach to solve
¹¹⁸ the magnetohydrodynamical (MHD) equations that govern the physics and evolution of re-
¹¹⁹ gions with magnetic fields. In recent years, significant progress has been made in areas like
¹²⁰ star formation and accretion disks through large-scale simulations, where researchers are now
¹²¹ confident in how magnetic fields might influence and change their host environments.
¹²²

¹²³ The presence of magnetic fields in the interstellar medium is still relatively unexplored.
¹²⁴ This medium lies between stars, is composed of dust, gas and radiation, and mainly serves as
¹²⁵ a fuel for star formation. Dying stars also pump energy back into this medium, and the gas
¹²⁶ structures are found to be largely complex and driven by turbulence. Magnetic fields in the

interstellar medium have been roughly estimated to be around a few μG . These fields are preserved by ionized plasma commonly found in the interstellar medium. Because of the chaotic nature of the interstellar medium, the field lines that thread it experience disturbances in the form of wave perturbations. These magnetic waves, also known as MHD waves, are of two types. The transverse waves are called the Alfvén waves. Alfvén waves propagate along the field lines, while the disturbance pushes plasma perpendicular to the magnetic field. An analogy to this is like disturbing a tight string from one end. The disturbance initiated at one end propagates to the other end with a signal speed, and material is disturbed perpendicular to the motion. So, inherently, magnetic field lines behave like strings.

The other type of waves is longitudinal MHD waves, known as magnetosonic waves. These waves are very similar to sound waves that propagate due to periodic compression and expansion of plasma density and magnetic field driven by increased thermal and magnetic pressure. There are two types of magnetosonic waves: fast and slow magnetosonic waves. Fast magnetosonic waves propagate in all directions, but are most often observed travelling perpendicular to field lines. As magnetic fields bring in additional stiffness to the interstellar medium, fast magnetosonic waves travel much faster than sound waves. Slow magnetosonic waves travel along the field lines but travel with the signal speed of the plasma medium. Studying the propagation and influence of these waves is crucial for understanding how energy is redistributed at large scales. These waves have been known to heat the interstellar medium, regulate star formation, act as a source of MHD turbulence and help us estimate magnetic fields. However, the structural and physical influence of MHD waves has not been fully understood. Due to the chaotic and turbulent nature of the interstellar medium, especially molecular clouds, both observationally and numerically, it has been a challenge to see the structural imprints of MHD waves on large-scale magnetic fields and their host environments.

Molecular clouds are known to have complicated hierarchical structures due to their largely turbulent nature (McKee and Ostriker, 2007; Federrath and Klessen, 2012; Padoan et al., 2014; Orkisz, Jan H. et al., 2017). Elongated and dense structures referred to as filaments have been observed across multiwavelength molecular cloud surveys (Molinari et al., 2010; André et al., 2014; Yuan et al., 2021). The structures of filaments are still under debate and have been proposed to be closer to ribbon-like or sheet-like structures (Auddy et al., 2016; Tritsis and Tassis, 2018). These dense structures harbour cores that serve as nurseries for active star-forming regions. Numerical and observational studies (André et al., 2014) examined the morphology of filaments and their role in the production of new stars. Large-scale ordered magnetic fields threading the dense filamentary structures have also been uncovered by polarimetric studies (Chapman et al., 2011; Planck Collaboration et al., 2016). These studies found that the direction of elongation of high-density regions is perpendicular to the direction of the ambient magnetic field. Therefore, their formation and dynamical evolution are proposed to be an interplay of turbulence, magnetic field, and gravity, where the large-scale magnetic field is usually perpendicular to the long axis of the filaments (Chapman et al., 2011; Planck Collaboration et al., 2016).

Although turbulence is suggested to be the major cause behind the existence of complex structures of molecular clouds, in the outer-diffuse regions, well-ordered, quasi-periodic, and

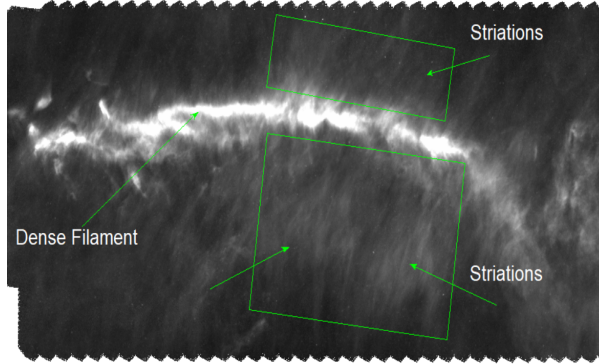


Figure 1.1: Striations observed in *Herschel* 250 μm dust emission map of Musca Molecular cloud. We see a dense filamentary structure in the middle. Striations are observed perpendicular to the dense structure and are well-aligned with Musca's plane-of-sky component (B_{pos}) of the magnetic field.

hair-like or thread-like structures, known as ‘striations’, were observed by Goldsmith et al. (2008) in the Taurus Molecular Cloud. Striations have later been found in several Molecular clouds such as Polaris Flare, Chamaeleon, Musca, L1624 and L914, to name a few (Miville-Deschénes et al., 2010; Panopoulou et al., 2016; Skalidis et al., 2023; Alves de Oliveira et al., 2014; Cox et al., 2016; Tritsis and Tassis, 2018; Malinen et al., 2016; Sun et al., 2024). These structures are also elongated like filaments but have low densities, and their long axes are well aligned with the plane-of-sky component of the background magnetic field (B_{pos}) threading the outer diffuse regions (Goldsmith et al., 2008; Chapman et al., 2011; Palmeirim et al., 2013; Alves de Oliveira et al., 2014). Across different molecular clouds, the number density estimates for striations range from 200 cm^{-3} to 1000 cm^{-3} , and the magnetic field strength for the outer regions has been estimated to vary from $10 \mu\text{G}$ to $120 \mu\text{G}$. Their strong alignment with magnetic fields and their quasi-periodic and anisotropic nature suggest that they are unlikely to form through turbulent interactions in molecular clouds.

Understanding the morphology, formation and evolution of striations has become a topic of growing interest. Their physical background can provide deep insights into the dynamics, evolutionary timescales and magnetic properties of the host molecular clouds. Several studies (Miville-Deschénes et al., 2010; Palmeirim et al., 2013; Alves de Oliveira et al., 2014; Cox et al., 2016; Malinen et al., 2016) have concluded that striations are linked to higher-density filaments at their roots. Flows along striations can be key in explaining the growth and evolution of the dense filamentary structures and can shed light on star-forming activities. For a long time, the pressure differences created by the fluctuating subsonic or supersonic flows along magnetic fields were considered the main mechanism behind the formation of striations (Miville-Deschénes et al., 2010; Palmeirim et al., 2013; Alves de Oliveira et al., 2014). Other physical processes, including Kelvin-Helmholtz instabilities (Heyer et al., 2016), MHD waves (Tritsis and Tassis, 2016; Heyer et al., 2016; Tritsis et al., 2018; Beattie and Federrath, 2020), corrugations of sheet-like structures (Chen et al., 2017), and anisotropic turbulent phase mixing (Xu et al., 2019), have been suggested to be the reason behind the formation of striations.

200 Figure 1.1 shows striations in the Musca molecular cloud in the *Herschel* 250 μm emission
201 map. Striations are connected to a dense structure. Polarimetric observations of Musca have
202 shown that these striations are well-aligned with the B_{pos} component of the magnetic field. Fig-
203 ure 1.2 displays the first observations of striations found in the northwest region of the Taurus
204 molecular cloud by Goldsmith et al. (2008). A recent ^{13}CO observation by Sun et al. (2024) of
205 striations from the L914 cloud in the Cygnus X region is also shown in Figure 1.2. Striations
206 are usually linked to a dense structure, as seen in Musca and L914. From the literature study
207 on striations, we find that they exist at different scales. Sun et al. (2024) revealed striations at
208 larger scales, while Goldsmith et al. (2008) has observed striations in much smaller regions in
209 the Taurus molecular cloud. The striations observed in Musca are of somewhat intermediate
210 size.

211
212 The pioneering study on the dynamics and formation of striations was conducted by Tritsis
213 and Tassis (2016), who performed several 2D and 3D ideal MHD simulations using FLASH.
214 They found that the coupling of incompressible and compressible MHD waves formed striations
215 with density contrasts and quasi-periodicity that matched the observed properties of striations
216 found in the Taurus molecular cloud. Regions surrounding the striations reflect and trap
217 compressive waves. The first application of the MHD wave theory and the formation of large-
218 scale normal modes were reported by Tritsis and Tassis (2018). They successfully inferred a
219 3D sheet-like structure of the Musca Molecular cloud by analyzing the spatial frequencies of
220 normal modes. By analyzing the propagation of the compressive fast magnetosonic modes,
221 Tritsis et al. (2018) calculated approximate periods of dominant wavemodes that explain the
222 evolutionary timescales of striations. Skalidis et al. (2023) found that the number densities of
223 striations and their presence in outer regions are ideal for the formation of molecular hydro-
224 gen and CO. MHD waves cause compression perpendicular to the long axis of striations, and
225 molecular gas formation is further enhanced.

226
227 However, these studies did not consider the presence of dense filamentary and sheet-like
228 structures and presented an isolated picture. The effect of gravitational potential creates a
229 stratified medium that can influence how striations form and evolve. Striations can explain
230 the involvement of magnetic fields, and flow along their long axes can help us understand the
231 formation and evolution of dense structures. High star-forming activities and the presence of
232 active cores can also dynamically influence striations. In the early stages of star-formation,
233 outflows and winds from protostellar disks continuously dump excess magnetic energy into
234 the outer diffuse regions (Wang et al., 2010). This makes active star formation a potential
235 source of MHD waves, including Alfvén waves that reach outer-diffuse regions. Kudoh and
236 Basu (2003) explored the influence of hydromagnetic waves in a stratified molecular cloud and
237 found standing-wave behaviour and longitudinal motions in outer regions. Although Tritsis
238 and Tassis (2016) explored the influence of MHD waves, a deeper look into the constant influx
239 of MHD waves and a stratified density atmosphere similar to Kudoh and Basu (2003) is needed
240 to understand the formation of striations by propagating MHD waves.

241
242 Because of their strong alignment with magnetic fields, striations are an excellent test
243 source for measuring magnetic field strengths. Davis (1951) and Chandrasekhar and Fermi
244 (1953) (Davis–Chandrasekhar–Fermi method or DCF method) and later Skalidis and Tassis

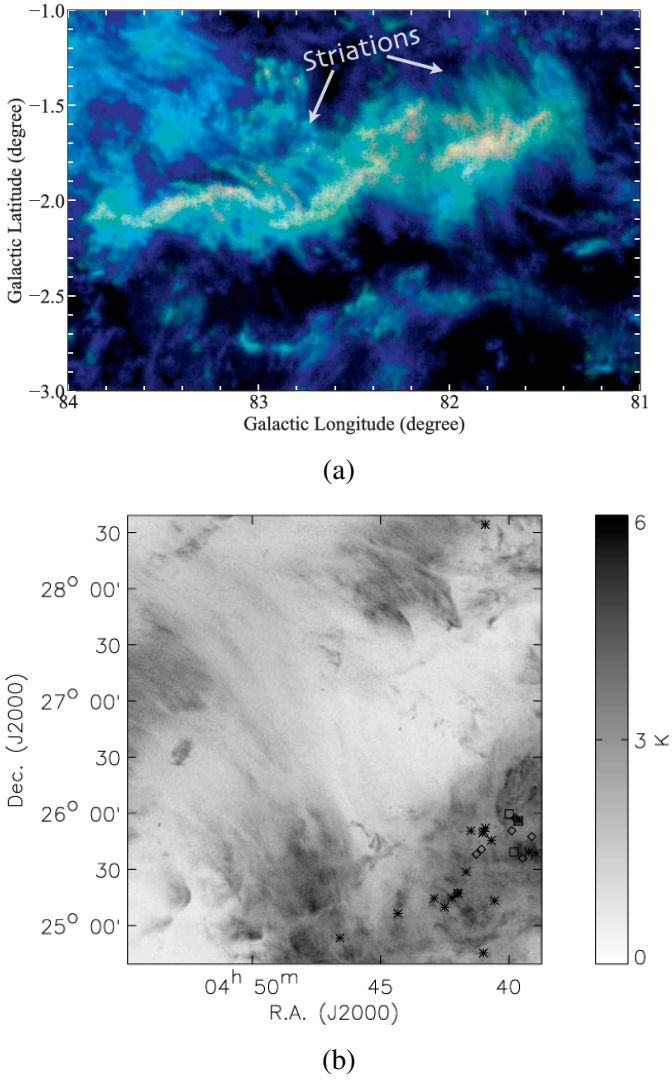


Figure 1.2: (a) We show a snapshot from Sun et al. (2024) of striations seen in the L914 molecular cloud present in the Cygnus X region in the ^{13}CO observations from the Milky Way Imaging Scroll Painting (MWISP) project. (b) The first observations of striations made by Goldsmith et al. (2008) in the northwest region of Taurus molecular cloud were detected in ^{12}CO emission. The squares, asterisks and diamonds indicate young stellar objects present in the denser regions.

(2021) (Skalidis-Tassis method or ST method) developed methods that have been employed to measure magnetic field strengths in molecular clouds. The main assumption of the DCF method is that the dispersion in magnetic fields is due to transverse Alfvén waves. The perturbations caused by these waves are seen as an unordered component causing fluctuations in the orientation of the magnetic field. However, in the ST method, the unordered component has been assumed to be the compressive modes aligned with the background magnetic field. Using the DCF method Skalidis et al. (2023) estimated magnetic field strength in certain regions in Polaris Flare, where striations are observed. They found that these regions have a magnetic field strength ranging from 38 to 76 μ G. In several regions of L914, Sun et al. (2024) estimated the magnetic field strengths B_{pos} to be in 47 to 88 μ G using the DCF method and 28 to 42 μ G using the ST method. Both methods are not in agreement with each other, and this stems from their conflicting core principles regarding the fluctuating component relative to the ordered component of magnetic fields. As striations are well-aligned with the background magnetic field and are not related to turbulence, a thorough understanding of the role of magnetic fields in their formation and evolution can help constrain estimates of magnetic field strengths in the outer regions. This will also help constrain the values of magnetic field strengths used in the numerical models exploring filamentary structures and star formation.

In this study, we further investigate the role of MHD waves in the formation of striations, both in a uniform medium and in a stratified medium resulting from the gravitational field of massive filamentary or sheet-like structures. Most dense filaments host many star-forming cores. These stellar cores send MHD perturbations, mainly Alfvén wave perturbations, into the outer regions. Due to density differences in these diffuse regions, Alfvén wave perturbations phase mix and dissipate their energy as magnetosonic modes travelling perpendicular to field lines (Nakariakov et al., 1997). Therefore, we introduce a source of Alfvén waves propagating into the molecular cloud. As striations tend to have higher-density roots and lower-density tails, they should be in a hydrostatic equilibrium with the gravity of the massive filament to which they are mostly connected. Hence, we carry out our investigation by introducing a stratified density profile into our simulations. We apply both the DCF and ST methods and calculate magnetic field strengths, and compare their applicability in outer regions of molecular clouds where both transverse and longitudinal wave modes are proposed to be present.

Chapter 2

Background

Transverse Alfvén waves experience phase mixing when sharp density fluctuations exist perpendicular to the direction of propagation. Nakariakov et al. (1997) found that phase mixing results in dissipation via compressive longitudinal waves under non-linear conditions. These compressive waves are fast magnetosonic waves, and their coupling with Alfvén waves depends on the strength of the density gradient perpendicular to the background magnetic field orientation and amplitude of Alfvén waves. This theory has been used to explain several physical aspects of solar physics (Parker, 1991; Nakariakov and Oraevsky, 1995).

Heyer et al. (2016), Skalidis et al. (2023) and Sun et al. (2024) found evidence of the compressive MHD waves. They were able to explain the quasi-periodicity of striations observed in diffuse regions of molecular clouds, which are parallel to the large-scale magnetic fields, and the wave periods also match the dynamical timescales for the formation of molecular gas due to magnetosonic compression. Tritsis and Tassis (2016) ran the 2D and 3D ideal MHD numerical models considering different mechanisms and found that propagation of compressive MHD waves as the only mechanism that can reproduce power spectra and density contrast closely resembling observations made in Taurus Molecular cloud and ruled out other physical phenomenon such as flows along the streamers and Kelvin-Helmholtz instabilities that were previously believed to be the main mechanisms behind striation formation.

Following the procedures derived by Nakariakov et al. (1997), we derive the 2D linearized MHD equations in the x and y directions. We assume no variations along the z-direction. We take the initial background field B_0 to be aligned in the y-direction and no component along the x-direction. In Section 3, we further discuss how we perturb the system with transversal Alfvén waves. The governing 2D MHD equations are

$$\frac{\partial \rho'}{\partial t} + \rho_0 \left(\frac{\partial v'_x}{\partial x} + \frac{\partial v'_y}{\partial y} \right) = N_1, \quad (2.1)$$

$$\frac{\partial B'_x}{\partial t} - B_0 \left(\frac{\partial v'_x}{\partial y} \right) = N_2, \quad (2.2)$$

$$\frac{\partial B'_y}{\partial t} - B_0 \left(\frac{\partial v'_x}{\partial x} \right) = N_3, \quad (2.3)$$

$$\rho_0 \frac{\partial v'_x}{\partial t} + \frac{B_0}{4\pi} \left(\frac{\partial B'_y}{\partial x} - \frac{\partial B'_x}{\partial y} \right) = N_4, \quad (2.4)$$

$$\rho_0 \frac{\partial v'_y}{\partial t} = N_5, \quad (2.5)$$

$$\frac{\partial B'_x}{\partial x} + \frac{\partial B'_y}{\partial y} = 0. \quad (2.6)$$

302

303 In Eq. 2.1 to 2.6 the variables v'_x , v'_y , B'_x , B'_y and ρ' are the perturbations in velocity, magnetic
 304 field and density, respectively, while the terms on the right hand side of each equation N_1 to N_5
 305 represents the higher-order non-linear terms. We perform a detailed theoretical analysis of the
 306 equations for our 2D model in Appendix A.

307

308

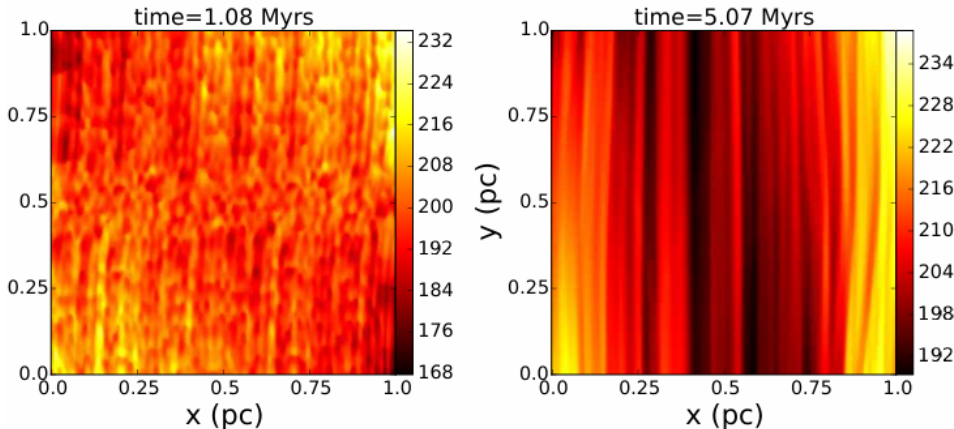


Figure 2.1: Slice number density maps from 2D ideal MHD simulations involving MHD waves performed by Tritsis and Tassis (2016). Striations start to form at around 1 Myr, and among all the physical mechanisms, MHD wave propagation achieved the density contrast closest to observations.

309 Tritsis and Tassis (2016) examined the coupling of Alfvén and magnetosonic waves based
 310 on theoretical findings made by Nakariakov et al. (1997). Their numerical setup included an
 311 Alfvén wave and a spectrum of Alfvén waves disturbing a uniform density medium (both at t
 312 = 0 Myr). To enhance coupling between Alfvén and magnetosonic modes, they added random
 313 density perturbations onto the density field, providing small but sharp density gradients. We
 314 show their results in Figure 2.1. Striations form after 1 Myr and continue to evolve until around
 315 5 Myr. They revealed that perturbing the system with a spectrum of Alfvén wave perturbations
 316 and increasing the amplitude improved the results in the density contrast of striations.

317

³¹⁸ Chapter 3

³¹⁹ Method

³²⁰ 3.1 Simulation Setup

³²¹ For our numerical setup, we use the ATHENA++ astrophysical code (Stone et al., 2020) to
³²² perform 2D MHD simulations. We apply an ideal MHD setup with self-gravity disabled and
³²³ magnetic fields enabled. The setup involves a uniform 2D Cartesian grid and a static mesh
³²⁴ algorithm. We employ a second-order van Leer predictor-corrector scheme to mitigate numer-
³²⁵ ical effects. For our results, we use a 256×256 cell resolution for all models. To confirm
³²⁶ convergence, we also run the simulations for a higher resolution of 512×512 cells (see Ap-
³²⁷ pendix A). Table 3.1 lists all the models we ran for different density profiles and magnetic field
³²⁸ strengths. The magnetic field values are listed as a ratio of Alfvén speed to isothermal sound
³²⁹ speed. We also show the values of plasma β parameter for each model, which is the ratio of
³³⁰ thermal to magnetic pressure and is equal to the ratio of the square of the speed of sound and
³³¹ Alfvén speed for the isothermal case (c_s^2/v_A^2).
³³²

³³³ 3.2 Initial Conditions

³³⁴ We define a Cartesian coordinate system in which a uniform magnetic field B_0 is oriented
³³⁵ along the y-axis, with no component existing along the x-axis. The computational domain is
³³⁶ 1 pc in each direction. We selected specific magnetic field strengths inspired by the observed
³³⁷ magnetic field strengths in striations around Musca ($\sim 12\mu G$), Taurus ($\sim 20\mu G$), and L914
³³⁸ ($\sim 40\mu G$) (Planck Collaboration et al., 2016; Chapman et al., 2011; Sun et al., 2024). We
³³⁹ assume isothermal conditions for our system, with a temperature around 15 K, motivated by
³⁴⁰ the observed temperatures in the outer parts of molecular cloud regions (Heyer et al., 2016;
³⁴¹ Tritsis and Tassis, 2016). On average, the number density of our setup is between 190 and 300
³⁴² cm^{-3} (Tritsis and Tassis, 2016). The initial configuration of our 2D setup is

$$B_y = B_0, \quad (3.1)$$

$$B_x = 0, \quad (3.2)$$

$$v_x = v_y = 0. \quad (3.3)$$

Table 3.1: Models (256^2 and 512^2 resolutions)

Model	v_A/c_s	plasma beta β	average number density (cm $^{-3}$)
Uniform Density Field	0.79	0.400	300
	1.58	0.100	300
	6.32	0.006	300
Stratified field under low gravity	0.79	0.400	299
	1.58	0.100	299
	3.16	0.025	299
	6.32	0.006	299
Stratified field under high gravity	0.79	0.400	190
	1.58	0.100	190
	3.16	0.025	190
	6.32	0.006	190

343

344

345 Random fluctuations are added to the density field uniformly in both directions, ensuring
 346 that the isothermality of the system is maintained. Initially, we present our study on a uniform
 347 density field, and later we introduce two stratified density profiles caused by the gravity of the
 348 filamentary structures that have been found linked with striations in many molecular clouds,
 349 and add a source of Alfvén wave perturbations (discussed further in Section 3.3). This mimics
 350 the Alfvén waves disturbances sent out by the active star-forming cores through outflows and
 351 stellar feedback into the outer regions where striations exist. Figure 3.1 shows the number
 352 density snapshot at the start of the simulation ($t = 0.0$ Myr) for the system under high gravity.
 353 Density perturbations can be seen as randomly distributed higher and lower density points.
 354 Initially, the physical properties of the cloud are

$$T(x, y) = T_0, \quad (3.4)$$

$$\rho(x, y) = \rho_0 + \delta\rho(x, y), \quad (3.5)$$

$$P(x, y) = P_0 + \delta P(x, y). \quad (3.6)$$

355 As Alfvén and slow magnetosonic waves can freely escape from the diffuse outer regions of
 356 the molecular clouds, we set an outflow boundary condition at the upper and lower boundaries
 357 of the 2D box. Alfvén waves get trapped and reflected by the surrounding high-density struc-
 358 tures in the molecular clouds (Tritsis and Tassis, 2018); hence, we choose reflective boundary
 359 conditions along the x direction. Higher-amplitude Alfvén disturbances propagate through the
 360 medium with random density perturbations and undergo phase mixing (initially coherent waves
 361 become out of phase). We believe this leads to strong nonlinear coupling between Alfvén and
 362 compressive MHD waves, providing ideal conditions to form striations (Nakariakov et al.,
 363 1997; Tritsis and Tassis, 2016; Heyer et al., 2016; Skalidis et al., 2023).

364

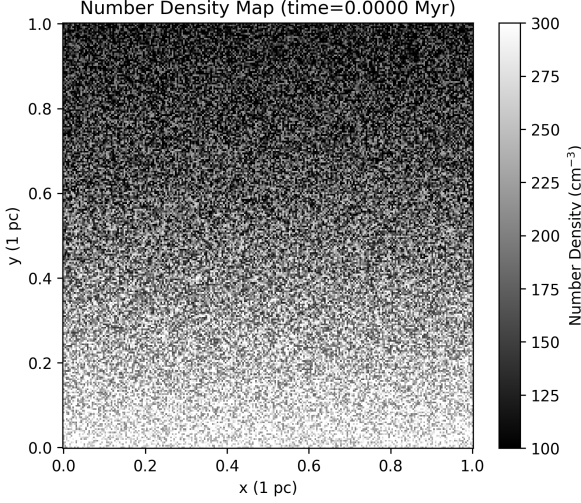


Figure 3.1: A snapshot of the number density at the start of the simulation. We maintain stratified density profiles that counterbalance the negative gravitational field (acting towards $y = 0$ pc boundary). Density white noise fluctuations are added to the background density field, seen as randomly distributed points spread across the 2D box.

365 3.3 New Boundary Conditions

366 We introduce two new boundary condition setups in ATHENA++. A constant negative gravitational field is added to the hydro solver for both the stratified density profiles. We maintain an
 367 exponential density profile throughout the cloud, ensuring it is in a perfect hydrostatic equilibrium.
 368 Ghost cells form a layer extending the main Cartesian computational grid in ATHENA++
 369 and ensure smoother flux reconstruction and transportation across the boundaries. We extend
 370 the density profile in the ghost cells region below the lower boundary ($y = 0.0$ pc) in the y
 371 direction to prevent the cloud's mass from flowing out of the system due to the negative grav-
 372 itational potential at the outflow boundary. We induce random density perturbations on the
 373 background density field, reaching a maximum amplitude $\delta\rho$ of 30 % compared to the initial
 374 density ρ_0 . Hence, the density profile for the gravitationally active clouds is
 375

$$\rho(y) = \rho_0 \exp\left(\frac{-y}{H}\right) \pm \delta\rho(x, y), \quad (3.7)$$

$$\rho(y_{ghost}) = \rho_0 \exp\left(\frac{-y_{ghost}}{H}\right), \quad (3.8)$$

$$H = \frac{c_s^2}{g}, \quad (3.9)$$

376 here H is the scale height defined as the ratio of the square of the isothermal sound speed
 377 c_s^2 to the gravitational field g . For the assumed initial isothermal conditions and number den-
 378 sity values, the isothermal sound speed is ~ 0.35 km/s, and we choose conservative values
 379 for the gravitational field lying between $\sim 10^{-7}$ to 10^{-8} cm s $^{-2}$. The scale height H for both
 380 the stratified density profiles range from 1 to 10 pc. We use the ghost cells layer at the lower
 381 boundary in the y direction as a source of Alfvén wave perturbations. We add high-amplitude

382 Alfvén waves that perturb the x component of the magnetic field, ensuring that the perturba-
 383 tion amplitude to the ordered magnetic field is always $\delta B/B_0 \simeq 0.1$. The frequency ω for the
 384 source Alfvén waves is set to be equivalent to the wave-crossing time for density waves across
 385 the 2D box ($1\text{pc}/c_s$) and, on average, remains similar across all the models. The perturbations
 386 are transported into the main computational domain box during the reconstruction phase and
 387 travel along the background field lines. The perturbations are sinusoidal in time. The inflow of
 388 Alfvén disturbances is maintained throughout the entire simulation. To eliminate numerical ar-
 389 tifacts and oscillations observed in simulations with strong magnetic field strengths, we switch
 390 on artificial isotropic viscosity in ATHENA++.

$$B_x(y_{ghost}) = \delta B \sin(\omega t), \quad (3.10)$$

$$\omega \simeq \frac{1\text{pc}}{c_s}, \quad (3.11)$$

$$\frac{\delta B}{B_0} \simeq 0.1. \quad (3.12)$$

Chapter 4

Results

We run 2D ideal MHD simulations in ATHENA++ for three different density profiles, ensuring a continuous influx of Alfvén waves throughout the entire cycle. Table 3.1 lists different density profiles and magnetic field strengths that we explore. To ensure strong coupling of Alfvén waves and fast magnetosonic modes, we maintain a ratio of amplitude of Alfvén waves δB to the background ordered field B_0 equal to 10% (Federrath et al., 2016; Tritsis et al., 2018) across all the simulations. This ensures consistency, and we were able to perform qualitative and quantitative comparison of how MHD waves behave in different initial magnetic field and density profiles in the nonlinear regimes.

All simulations are run until the magnetosonic modes gradually fade out due to numerical dissipation. In Section 4.1, we discuss that the uniform density field achieves and maintains a stable configuration for longer durations. However, over the entire timescale, magnetosonic waves do not effectively change the structural properties of striations. As we introduce a stratified atmosphere through a constant gravitational field in Section 4.2 and 4.3, we observe that striations form early in the cloud. The propagating magnetosonic waves coagulate the small-scale density compressions into large-scale high-density regions, resulting in high density contrast. We discuss the results and insights found from each density profile in much more depth in the next sections.

4.1 Uniform Density Field

The first case we simulate is the cloud with a uniform density field. We choose three different initial magnetic field strengths as listed in the Table 3.1. As observed by Federrath et al. (2016) and Chapman et al. (2011), we chose the ratio of amplitude of Alfvén wave perturbations (unordered) δB to the initial background magnetic field (ordered) B_0 to be 0.1. Initially, the cloud has average density ρ_0 equal to 300 cm^{-3} . We add the random density white noise perturbations isotropically throughout the cloud. The source of Alfvén waves exists in the ghost cells as discussed in section 3. In Figure 4.1, we show the number density slice maps at three time steps, approximately 3, 5, and 7 Myr after the evolution. The strength of the magnetic field increases as we move from the top to the bottom row in Figure 4.1.

422 Adjacent low-density and high-density elongated and ordered striations, well-aligned with
423 the background magnetic field B_0 , form after 3 Myr for each magnetic field strength. The spac-
424 ing and structure of striations are similar to those Tritsis and Tassis (2016) found in their 2D
425 ideal MHD simulations with an initial Alfvén wave perturbation and not a continuous source
426 of Alfvén waves. As we increase the magnetic field strength, we observe that striations form
427 earlier compared to the weak magnetic field. We follow the same approach as in Tritsis and
428 Tassis (2016) to measure the mean density contrast between the adjacent rarefied and com-
429 pressed regions. The mean density contrasts for the weak, medium and strong magnetic field
430 strengths lie between 9 to 11 %, which is higher than the estimated mean density contrast of
431 4 to 7 % seen in the 2D models in Tritsis and Tassis (2016). This means that the coupling of
432 Alfvén and fast magnetosonic mode gets stronger as we increase the magnetic field strengths,
433 and more energy is dissipated into the fast magnetosonic modes (Nakariakov et al., 1997).

434
435 After 5 Myr, some large-scale regions of the cloud have higher densities seen for each
436 magnetic field strength. This is an aftereffect of large-scale compression, and the other areas
437 experience density reduction. As noted by the peaks in number density power spectra shown
438 by Tritsis and Tassis (2016) and Tritsis et al. (2018), the power redistributes to small wavenum-
439 bers or frequencies, indicating that power is dumped onto larger wavelengths corresponding to
440 larger scales. The compressive fast magnetosonic waves continue to propagate perpendicular
441 to the background magnetic field, compressing large sections of the cloud parallel to the long
442 axis of striations and B_0 . These compressive waves slowly lose energy and dissipate due to
443 numerical dissipation after repeatedly reflecting from the reflective boundaries along the x-
444 direction. Therefore, striations slowly fade away, and the cloud eventually turns back uniform.
445 Hence, after 7 Myr of evolution, the cloud has regained a relatively uniform density as seen in
446 panel (c) in Figure 4.1.

447
448 Although power redistributes to large-scale regions, the structure of striations doesn't seem
449 to be affected by compressive magnetosonic waves. There is strong evidence that fast mag-
450 netosonic waves interact and form normal modes. These modes successfully explained the
451 quasiperiodic nature of striations (Tritsis and Tassis, 2018; Tritsis et al., 2018). In Figure 4.2,
452 number density and velocity power spectra for the medium magnetic field strength model are
453 shown at 5 Myr of evolution. We observe peaks at small spatial frequencies for both the num-
454 ber density and velocity, consistent with those observed by Tritsis and Tassis (2016) and Tritsis
455 et al. (2018) at smaller spatial frequencies in their MHD simulations. The peak at small spatial
456 frequencies corresponds to the width of the 2D simulation box ($\sim L_x$). Tritsis and Tassis (2018)
457 found that the peaks in column density power spectra should define the power distribution of
458 the fast magnetosonic normal modes, causing large-scale density compression, which we do
459 not observe in the uniform density simulations.

460
461 Active star formation persists for only a few Myrs (André et al., 2014; Kumar et al., 2020).
462 Striations in a uniform-density field appear to persist for much longer than the active star-
463 formation timescales; they exist for timescales closer to the lifetimes estimated for molecular
464 clouds of 10 Myr (Kumar et al., 2020). Lack of observational samples of striations suggests
465 they may be short-lived transient structures that appear only at the initial stages of filamentary
466 cloud formation (Sun et al., 2024). The filamentary regions that interconnect striations have

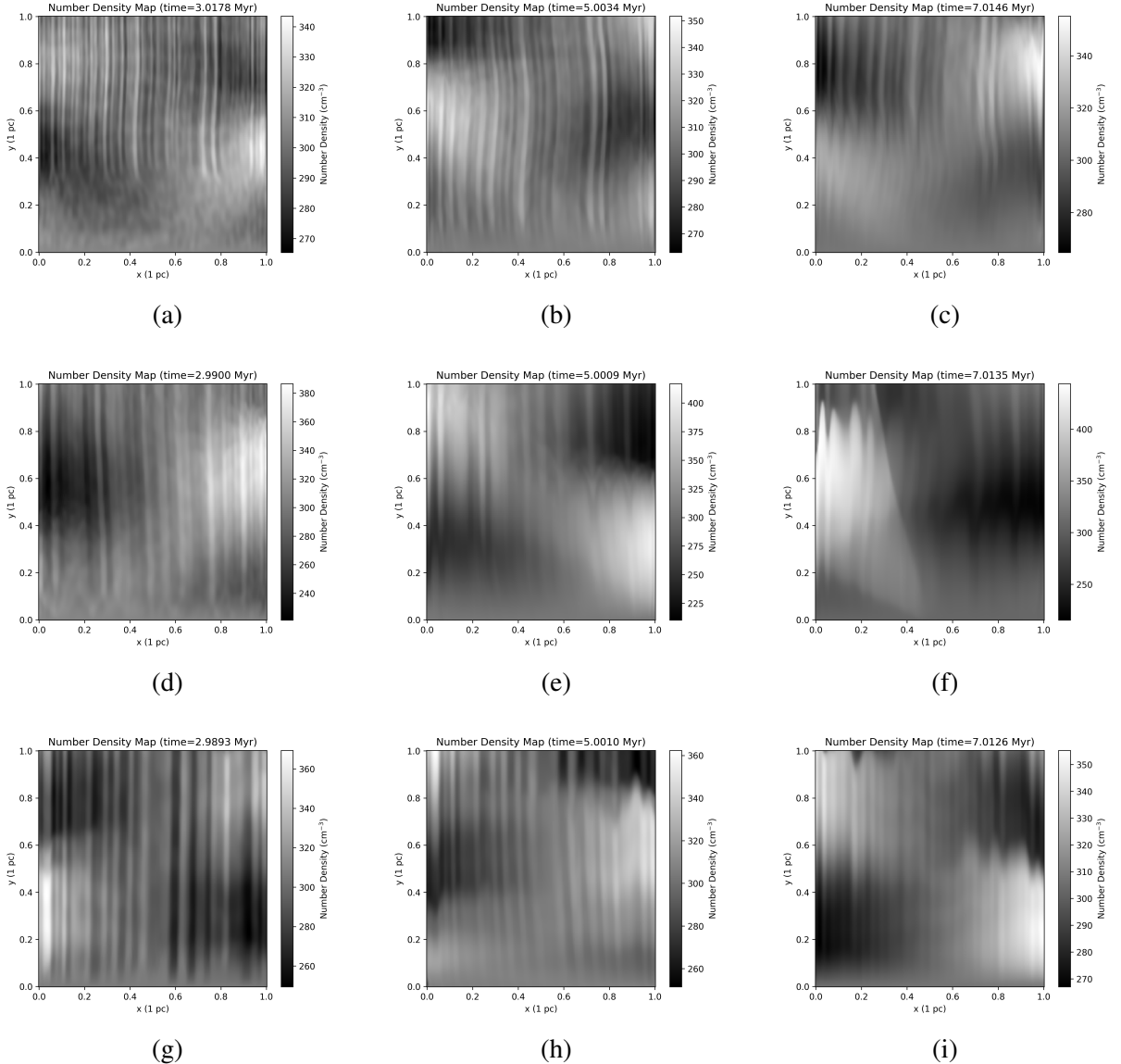


Figure 4.1: Number density slice maps from the 2D ideal MHD simulations for a uniform density field at different time steps and initial magnetic field strengths. The first row shows density maps from the weak magnetic field simulations; the second row shows density maps from the medium magnetic field simulations; the last row shows the number density plots from the strong magnetic field simulations.

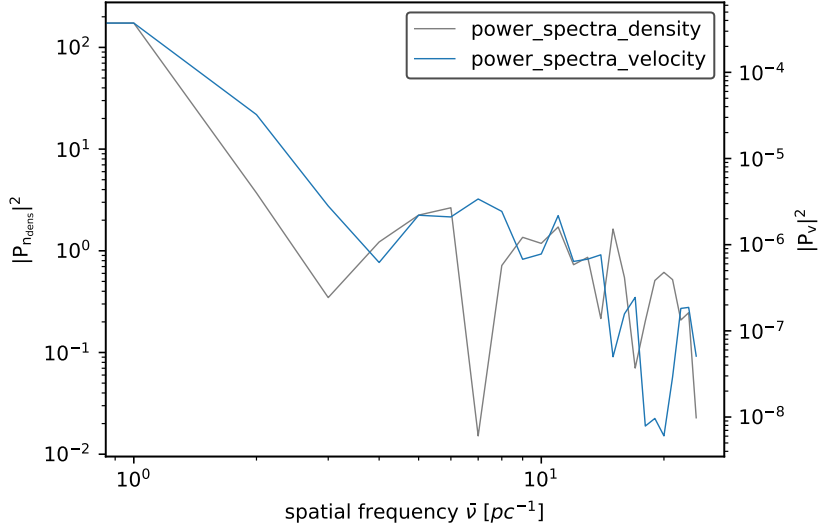


Figure 4.2: Number density (n) and velocity (v) spatial power spectra for medium magnetic field strength with a uniform density field after 5 Myr of evolution. The spectra are computed at the midplane ($y = 0.5$ pc) by taking a cut perpendicular to the background magnetic field B_0 .

significantly higher mass than the low-density outskirts. A weak gravitational field acts on the low-density outer regions of the cloud, yet its dynamical influence has not been incorporated in the uniform-density simulations. Density reduces along the long axis of striations, starting from higher-density roots to lower-density tails, resulting in a weak density gradient. Therefore, in the next two sections, we explore the evolution of the cloud in a hydrostatic balance against the gravitational field.

473

474 4.2 Stratified field under low gravity

475 We again assume a number density n around 300 cm^{-3} and a weak constant gravitational field
 476 with $g = 0.1$ in ATHENA++ code units and is close to $10^{-8} \text{ cm s}^{-2}$ in physical units. The scale
 477 height H is around ~ 10 pc for this case. The volume density at the bottom boundary ρ_0 for the
 478 given assumed number density (300 cm^{-3}) is around $1.17 \times 10^{-22} \text{ g cm}^{-3}$. We plot the number
 479 density slice maps for the weak gravity case in Figure 4.3, similar to the Figure 4.1. Under a
 480 gravitational field and a stratified density profile, the evolution of the cloud and striations has
 481 changed drastically. Therefore, we have taken the number density slice maps at 1, 2.5 and 4
 482 Myr as shown in Figure 4.3. We see in the panels Figure 4.3(a), (d) and (g), small-scale high-
 483 density regions appear after 1 Myr for each magnetic field strength.

484

485 This transformation occurs at a much earlier stage compared to the uniform density, which
 486 took around 3 Myr for striations to form. The small-scale striations are well-aligned with the
 487 background magnetic field and are isotropic throughout the cloud. We anticipate that these
 488 small scales form uniformly across the 2D box because of the initial small-scale random den-
 489 sity fluctuations. The compressions at small scales are a result of magnetic pressure exerted by

490 fast magnetosonic waves that originate through phase-mixing of Alfvén waves. Phase-mixing
491 is ensured by sharp density gradients transverse to the background magnetic field (Nakariakov
492 et al., 1997). Localized sharp density gradients are a byproduct of random density fluctuations
493 that create small but sharp density fluctuations in neighbouring grid cells.

494
495 Unlike uniform-density field models, in stratified-density field models, striations are in-
496 fluenced by propagating fast magnetosonic waves. The panels (b), (e) and (h) in Figure 4.3
497 (corresponding to weak, medium and strong magnetic field strengths, respectively) show the
498 number density maps at 2.5 Myr. In each panel, a large region of the cloud has been compressed
499 near the right boundary of the 2D box. The compressed areas have elongated striations, and at
500 this stage, both the small-scale and elongated striations coexist in the cloud. The mean density
501 contrast for the low-gravity field is around 3 %, which is lower than the uniform density. How-
502 ever, we also measure the density contrast on large scales between the compressed and rarefied
503 regions along the cuts perpendicular to the background magnetic field.

504
505 To measure the density contrasts between the compressed and rarefied regions, we take
506 perpendicular cuts at different heights in the cloud. To improve signal-to-noise, we average out
507 the number density values with three adjacent cuts parallel to the main cut. Along these cuts,
508 we identify the regions near the two density extremes. Further, we compute the density contrast
509 along each perpendicular cut in the two regions and compute an average value. We estimated
510 that the density contrasts between the two contrasting regions for the weak, medium and strong
511 magnetic fields are around 11, 28 and 21 %, respectively and are close to the observations (Sun
512 et al., 2024; Skalidis et al., 2025) where the density contrast on large scales is within 15 to 40
513 %. Additionally, in this model, striations vary in length and mean width, unlike the uniform
514 case, where they largely preserve their structural properties throughout evolution.

515
516 Striations in the weak magnetic field simulations remain largely uniform even at the late
517 stage of evolution, as seen in Figure 4.3(c). The cloud experiences the lowest density contrast
518 (11 %) among the three magnetic field strengths. However, in the medium magnetic field sim-
519 ulations, we observe the highest density contrast of 28 %. We notice stronger compression
520 near the right boundary in Figure 4.3(e) than seen in Figure 4.3(b). The density contrast in the
521 two extreme regions has increased by more than a factor of two as we increased the magnetic
522 field strength. A stronger background magnetic field means higher-amplitude perturbations
523 ($\delta B/B \simeq 0.1$) and higher Alfvén speeds. Higher propagation speeds allow the Alfvén waves
524 to travel further and enable efficient coupling between Alfvén waves and fast magnetosonic
525 compressive waves. The first peak in the power spectra shown in Figure 4.4 corresponds to
526 magnetic energy stored in the large-scale compressed region at 2.5 Myr.

527
528 The cloud with initially the strongest magnetic field strength shows the earliest sign of com-
529 pression as seen in the lower-right section of Figure 4.3(g). In this case, we see that multiple
530 large-scale compressive magnetosonic waves have formed independently in the lower and up-
531 per half of the cloud, as shown in Figure 4.3(h), due to the difference in propagation speed.
532 These waves travel out of phase with each other, causing the cloud to be compressed at oppo-
533 site sides at different heights. Gradually, the waves enter a synchronous motion, resulting in a
534 much larger compressed region caused by the magnetic pressure of the magnetosonic waves,

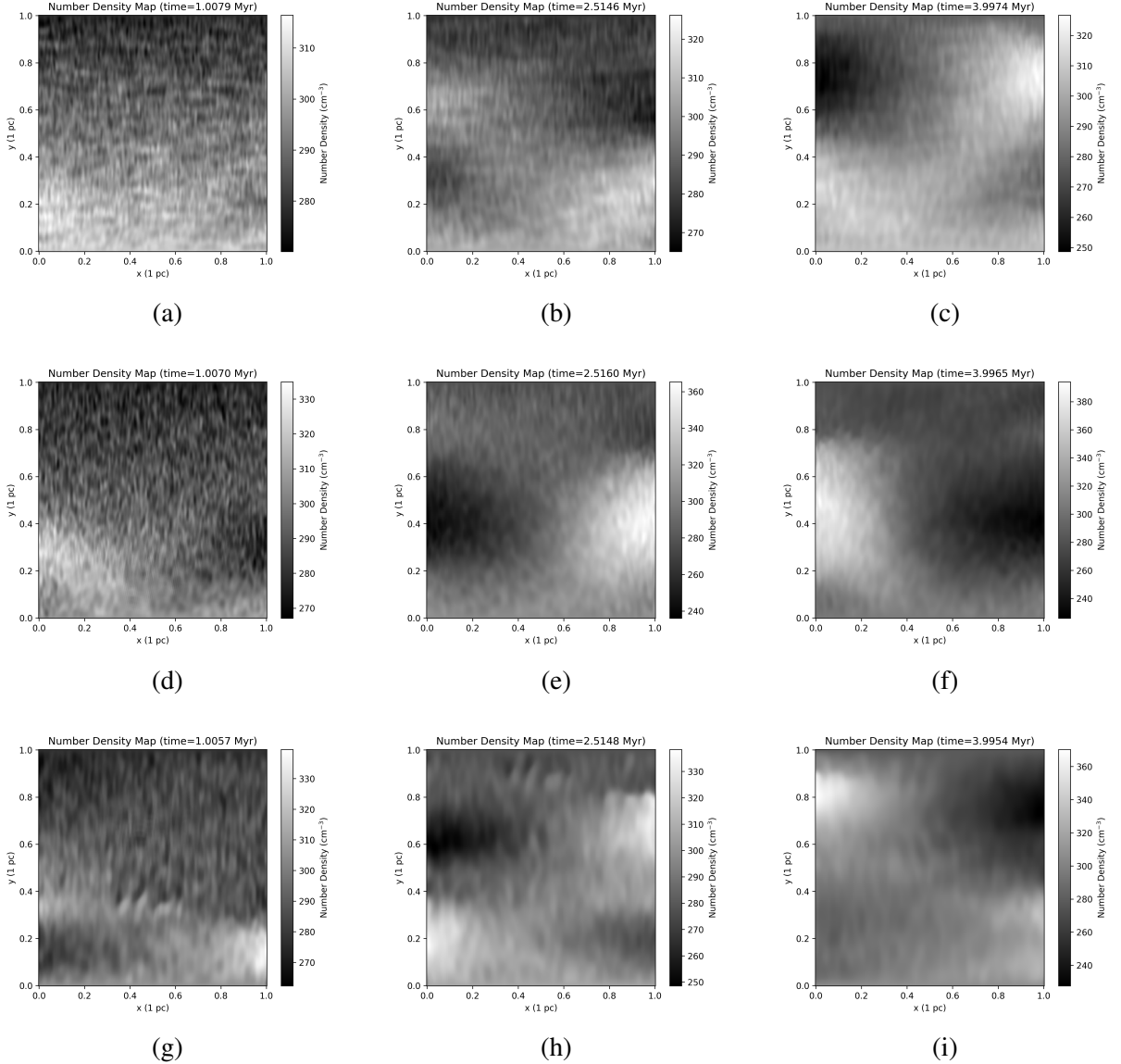


Figure 4.3: Similar to Figure 4.1, number density slice maps are shown for the stratified density field under low gravity for three different magnetic field strengths. The magnetic field strength increases from the top to the bottom rows, with the top being the weakest and the bottom row being the strongest.

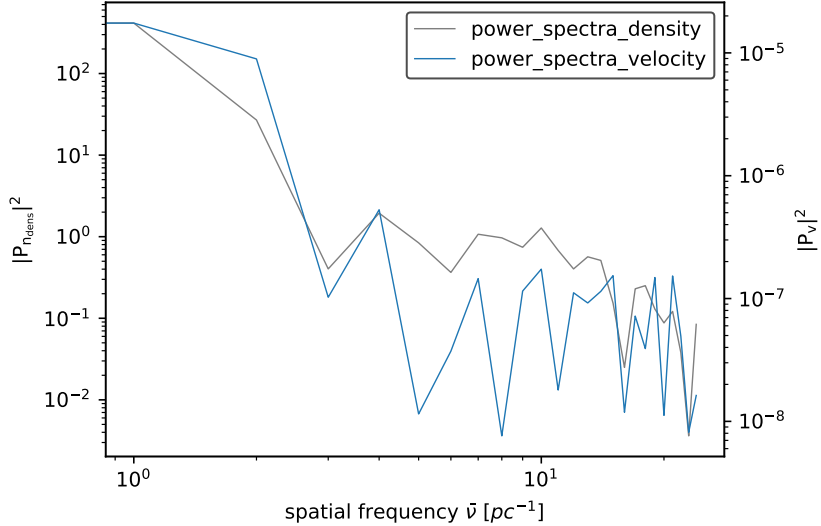


Figure 4.4: Similar to Figure 4.2, spatial power spectra for number density and velocity field at the midplane are shown at 2.5 Myr for the stratified density field model with medium magnetic field strength.

and a low-density region forms on the opposite side. Although strong magnetic fields and high-amplitude Alfvén perturbations should imply stronger coupling between Alfvén and fast magnetosonic waves as seen in the medium magnetic field case, we find that the density contrast between compressed and rarefied regions has dropped to 21% compared to 28% estimated in the medium magnetic field simulation. Physically, this means that the fast magnetosonic waves cannot create a magnetic pressure gradient that is significant enough to compress the stronger background magnetic fields, thus resulting in relatively lower density contrasts.

542

Overall, in the low-gravity stratified density atmosphere model, we simulated regions relatively close to the high-density regions associated with dense structures due to their larger scale height. Power spectra of the cloud still closely resemble numerical simulations and observations for both number density and velocity (Tritsis et al., 2018; Tritsis and Tassis, 2018), and we again see peaks at the low spatial frequencies in the Figure 4.4 after 2.5 Myr of evolution. In Figure 4.3, we see how compressive fast magnetosonic modes influence the structural properties of the cloud, a phenomenon not previously observed in numerical simulations (Tritsis and Tassis, 2016; Tritsis et al., 2018). Small-scale striations form in all simulations with different initial magnetic field strengths under a constant gravitational field, but their evolution and growth depend on the strength of the background magnetic field and MHD waves. We noticed that for weaker magnetic field strengths, the Alfvén waves do not efficiently couple into fast magnetosonic modes, and the striations remain densely packed and uniformly distributed until very late stages. As we increase the magnetic field strength ($v_A/c_s > 2$), fast magnetosonic waves appear early on and exert efficient magnetic pressure parallel to the background magnetic field, compressing field lines.

558

4.3 Stratified field under high gravity

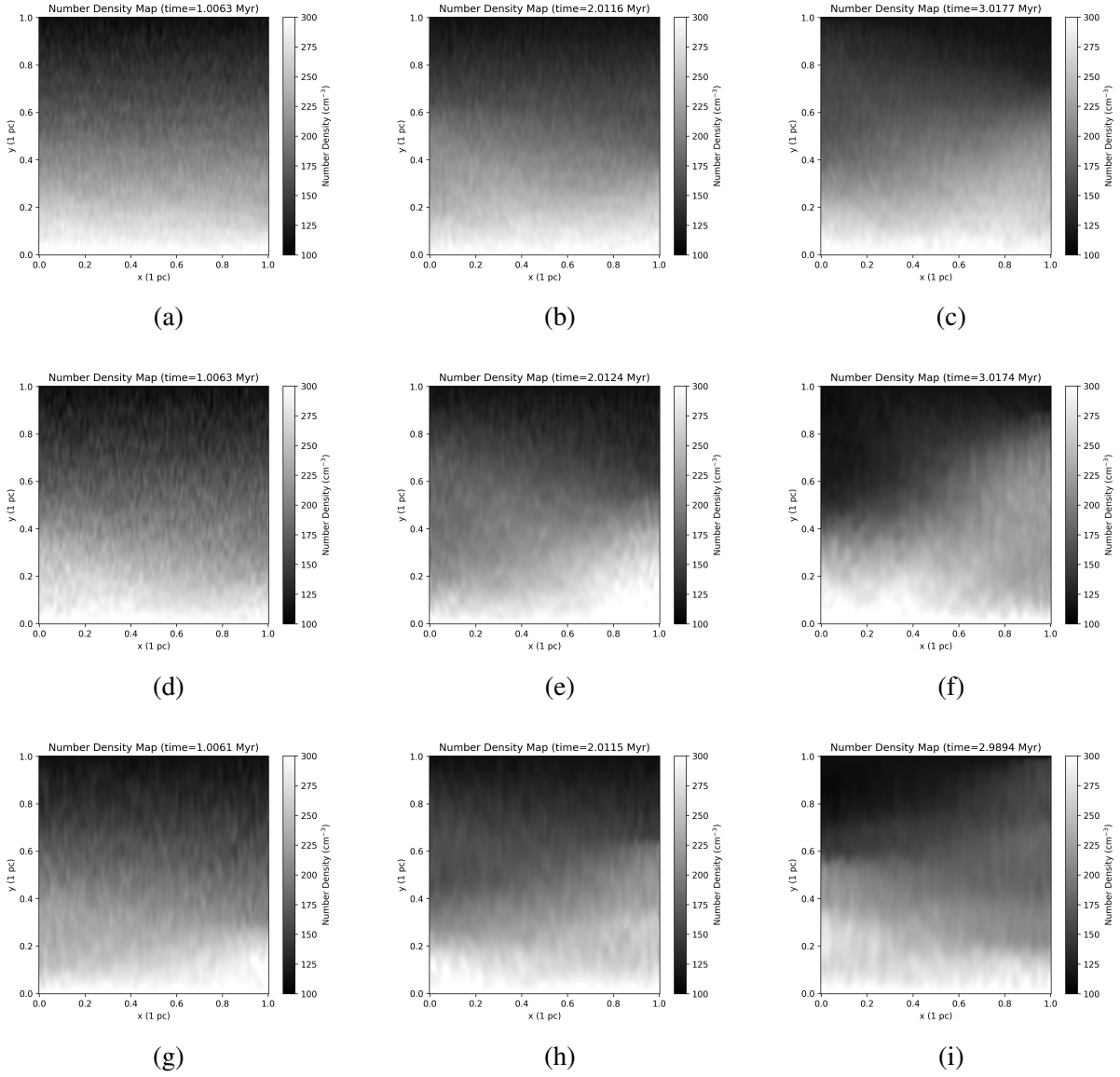


Figure 4.5: Similar to Figure 4.3, 2D number density slice maps are shown for the stratified density field model under high gravity for three different magnetic field strengths.

We run 2D ideal MHD simulations with a setup similar to that in Section 4.2, but now with a stronger gravitational field, $g = 1.0$ in ATHENA++ code units, equivalent to $10^{-7} \text{ cm s}^{-2}$ in physical units. Since the cloud has the same initial temperature and isothermal conditions, the isothermal sound speed c_s remains the same, and the new scale height approaches $H \simeq 1 \text{ pc}$. This results in density dropping from $\rho_0 (1.17 \times 10^{-22} \text{ g cm}^{-3})$ at the bottom boundary to $\sim \rho_0/e$ near the upper boundary, giving a strong density gradient along the y-direction. We keep a source of Alfvén waves and perform simulations with the magnetic field strengths as mentioned in Table 3.1.

Similar to the low gravity density field simulations, we observe that under high gravity and a stronger density gradient, the striations form at small scales, as seen in Figures 4.5(a), (d), and (g) for all the magnetic field strengths. The striations in the cloud with a weak magnetic field do not evolve any further, and the system largely remains isotropic till 3 Myr. This indicates that the fast magnetosonic waves either did not appear or were dissipated early on. This is an effect of inefficient coupling of Alfvén and fast magnetosonic waves due to low amplitudes and Alfvén speeds resulting from the weak magnetic field. Also, because the influx Alfvén disturbances have lower amplitudes, we anticipate that the waves lose energy in the high-density regions of the cloud near the $y = 0$ pc boundary due to the strong density gradient along the y direction. This results in weak Alfvén flux reaching higher into the molecular cloud, which gets dissipated by numerical effects. As a result, we observe no anisotropic large-scale compressed and rarefied regions of the cloud in the weak magnetic field model. Striations on smaller scales have been observed in Musca and Taurus (Chapman et al., 2011; Goldsmith et al., 2008; Heyer et al., 2016). We believe small-scale striations may be associated with weaker magnetic fields, or it could be that they have formed in the initial stages of their filamentary molecular cloud evolution.

For medium magnetic field strength, we increase the amplitude of the disturbances to satisfy the imposed condition of $\delta B/B \simeq 0.1$. This ensures efficient coupling between Alfvén and magnetosonic modes as observed in the results from Section 4.1 and 4.2. Small-scale structures form after 1 Myr, and as we evolve the system for another million years, the compression imprinted by the fast magnetosonic waves is evident in Figure 4.5(e). We observe a higher density region and elongated striations at the right corner of the simulation box. Alfvén waves dissipate initially in the lower parts of the clouds, as they are directly transported from the ghost cells. Gradually, higher-amplitude perturbations propagate into the upper low-density regions in the cloud and dissipate as fast magnetosonic modes. Eventually, after 3 Myrs of evolution as seen in Figure 4.5(f), a much larger section of the cloud has been compressed near the right reflective boundary in the x -direction. We see that highly elongated, well-aligned striations have formed in that region, and the other half of the box shows a drop in the density. The density contrast between the two high and low-density regions is around 34 %, which is the highest among all the models and also matches the observations discussed in section 4.2. The cloud becomes highly anisotropic, and propagating fast magnetosonic modes introduce a periodicity (with wavelength $\lambda_{ms} \sim 2L_x$) to the anisotropic behaviour. The same behaviour and structural shift have been observed by Tritsis and Tassis (2018) for Musca molecular cloud on relatively larger scales.

Compressive fast magnetosonic waves are also seen to be efficiently produced in the strongest magnetic field case. In this model Alfvén waves perturbations propagate at higher Alfvén speeds, and the presence of random density fluctuations ensures that coupling between the transverse and longitudinal modes occurs early in the molecular cloud. We observe in Figure 4.5(h) that compressed and rarefied regions have appeared after 2 Myr, similar to the medium magnetic field strength as seen in Figure 4.5(e). However, as observed in the low gravity stratified density models for a strong magnetic field, the maximum density contrast decreases (25 %) compared to the medium magnetic field case. This again hints at the picture that although compressive fast magnetosonic waves are dissipated, the magnetic pressure induced cannot push or com-

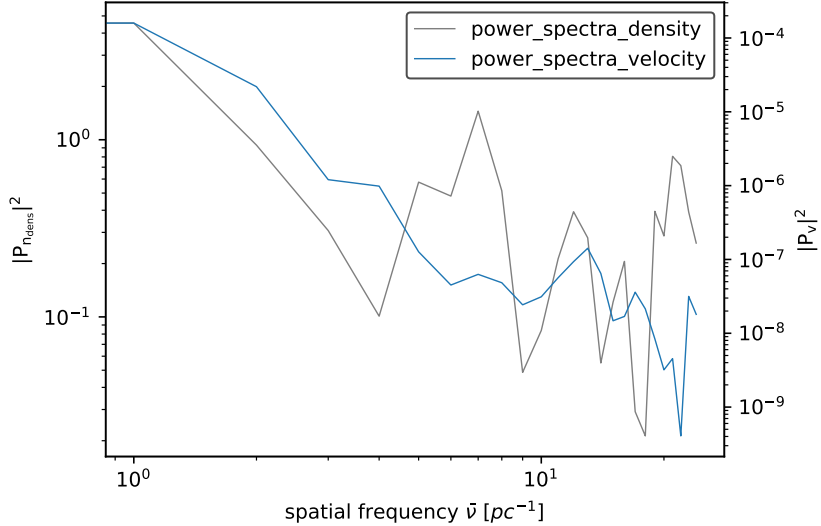


Figure 4.6: Similar to Figure 4.2, spatial power spectra for number density and velocity are plotted at the midplane at 2 Myr for the stratified density field under high gravity.

press the strong magnetic field lines. In the next sections, we examine the influence of different magnetic field strengths on the evolution of both transverse and longitudinal MHD waves by studying the different physical properties of the cloud.

4.4 Influence of MHD waves

The 2D model with a medium magnetic field and stratified density profile under high gravity experienced the strongest fast magnetosonic compressions. Of all the models, it achieved the highest density contrast of 34 % between the compressed and rarefied regions. Therefore, for quantitative and qualitative analysis of the propagation of fast magnetosonic waves, we choose 2D ideal MHD simulations with the strongest gravitational field and an initially medium magnetic field strength for further analysis and comparisons. Figure 4.7 and Figure 4.8 show the number density n and the magnetic field's y-component B_y slice maps at 3 Myr and 4 Myr, respectively.

In Figure 4.7, the aftereffects of fast-magnetosonic compressions are visible in both 2D slice maps of number density and the magnetic field's y component B_y . In Figure 4.7(a), at 3 Myr, the fast magnetosonic wave has caused a large region of the molecular cloud to be compressed near the right reflective boundary of the box. Figure 4.7(b) highlights that the same region experiences an increase in magnetic field strength in the B_y component, which is caused by the magnetic pressure imposed by fast magnetosonic waves ($B_y^2/8\pi$). The pressure acts parallel to the background field, causing a sudden increase in the number density and magnetic field strength near the right boundary of the cloud. On the contrary, the region closer to the left reflective boundary experiences a drop in the average number density and magnetic field strength. Figure 4.7 provides concrete evidence that eventually the large-scale

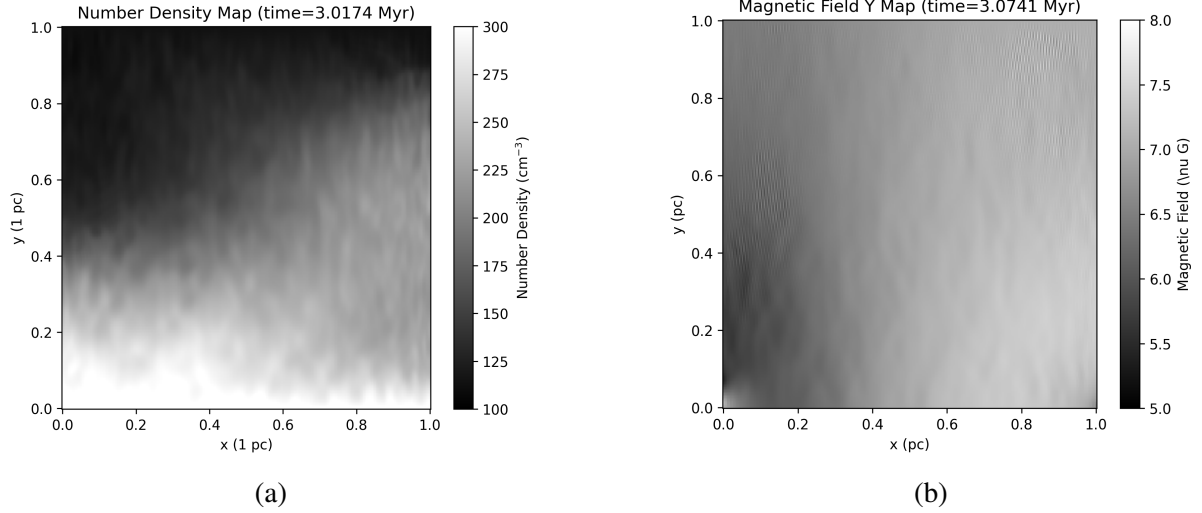


Figure 4.7: Comparison of (a) number density n map with (b) B_y magnetic field map for the high-gravity stratified density profile and medium magnetic field conditions at ~ 3 MYr. Fast Magnetic waves propagate and create magnetic compression near the right boundary of the 2D computational box. This results in peaks in both number density and magnetic field around that region, while the opposite region near the left boundary experiences rarefaction.

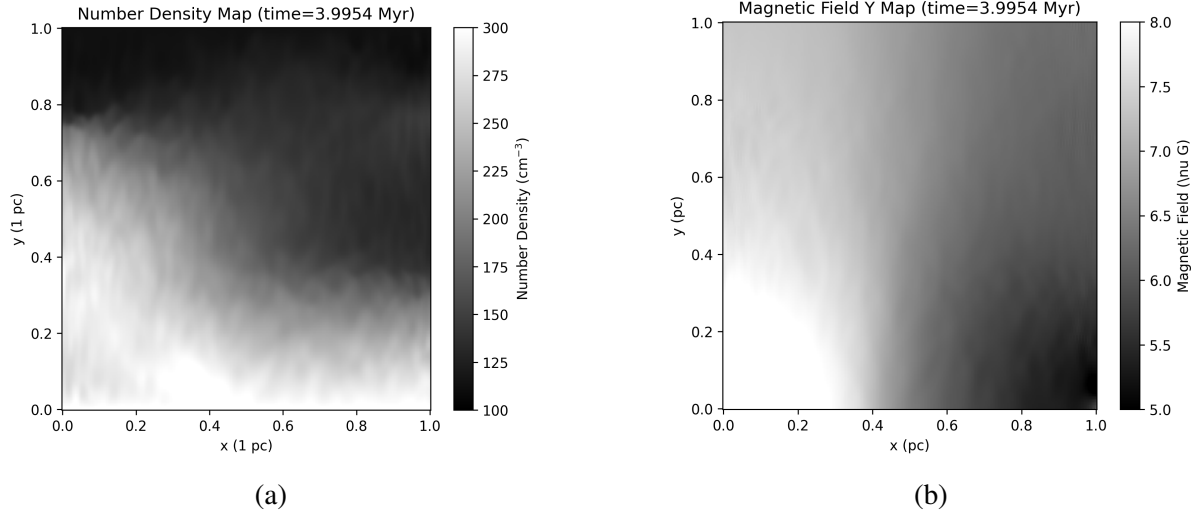


Figure 4.8: Comparison of (a) number density n map with (b) B_y magnetic field map for the high-gravity stratified density profile and medium magnetic field conditions at ~ 4 MYr. similar to Figure 4.7, we again observe compression in both density and magnetic fields, but near the left boundary of the 2D box and with increased intensities.

638 compressive MHD modes influence the system, and regions with higher number density and
639 magnetic pressure result from compression driven by the propagating fast magnetosonic waves.

640

641 This is enhanced further at around 4 Myr, as seen in Figure 4.8. Continuous influx of
642 Alfvén waves dumps more energy into the system as fast magnetosonic waves, which are
643 trapped and continuously propagate throughout the cloud. The large-scale fast magnetosonic
644 modes reflect at some point between 3 and 4 Myr and reach the left-end boundary of the 2D
645 box. This results in compression near the left boundary of the system, opposite to the com-
646 pression observed in Figure 4.7. Consequently, at 4 Myr, the magnetic pressure increases the
647 number density near the left boundary of the cloud and similarly increases the B_y component
648 of the magnetic field. For these conditions, the cloud maintains efficient coupling between
649 Alfvén waves and fast magnetosonic modes throughout its evolution. On larger scales, obser-
650 vations have revealed highly elongated striations existing in L914, Musca, and Polaris Flare
651 (Skalidis et al., 2023; Sun et al., 2024; Tritsis and Tassis, 2018).

652

653 To see how compressive waves affect the physical properties of the cloud, for each model,
654 we take a perpendicular cut at the midplane $y = 0.5$ pc, and calculate the normalized number
655 density $n_{\text{density}}(x)/n_0$, where n_0 is the average number density of the cloud. For the models with
656 stratified density profile, n_0 is the average number density near the bottom boundary ($y = 0$
657 pc). In Figure 4.9, we plot the normalized number density for the three density profiles for the
658 models with a medium magnetic field. For the high-gravity stratified density field shown in the
659 left panel 4.9(a), we find that until around 2 Myrs, the small-scale coupling persists, creating
660 localized peaks and troughs in normalized number density. However, after about 3 Myr, these
661 small-scale fast magnetosonic waves have sufficient time to reflect and superimpose, result-
662 ing in large-scale normal modes which influence the cloud on large scales. The normalized
663 number density of the cloud peaks near the right boundary, while the other boundary experi-
664 ences the lowest density throughout the cloud. It clearly matches the cloud's structural change
665 captured in Figure 4.7, where large-scale fast magnetosonic modes have caused significant ma-
666 terial compression near the right boundary of the box.

667

668 The observed contrast between the highest and lowest points at the midplane is around
669 30%. For medium magnetic field strength, the normalized density plot for the low-gravity
670 stratified density profile is displayed in Figure 4.9(b). This model experiences a strong influ-
671 ence of MHD compression at both 2.5 and 4 Myrs, achieving a maximum density contrast of
672 47 %. The normalized density plots for the uniform density case also show the effects of mag-
673 netic compression. However, we don't see any evidence of large-scale structural change in the
674 orientation and shape of striations in its number density maps (see bottom row of Figure 4.1).

675

676 Figure 4.10 and Figure 4.11 plot the normalized number density plots for models with
677 weak and strong magnetic field strength, respectively. Fast magnetosonic waves are found to
678 be dissipated due to phase-mixing of Alfvén waves in both magnetic field strengths. However,
679 their compressive effects are weaker than those detected in the medium magnetic field models.
680 Mild compression is evident early on in the low-magnetic field case for each density profile
681 as seen in Figure 4.10. Because of the weak magnetic field strength and smaller amplitude
682 Alfvén waves, the dissipated fast magnetosonic waves have less power. Therefore, the maxi-

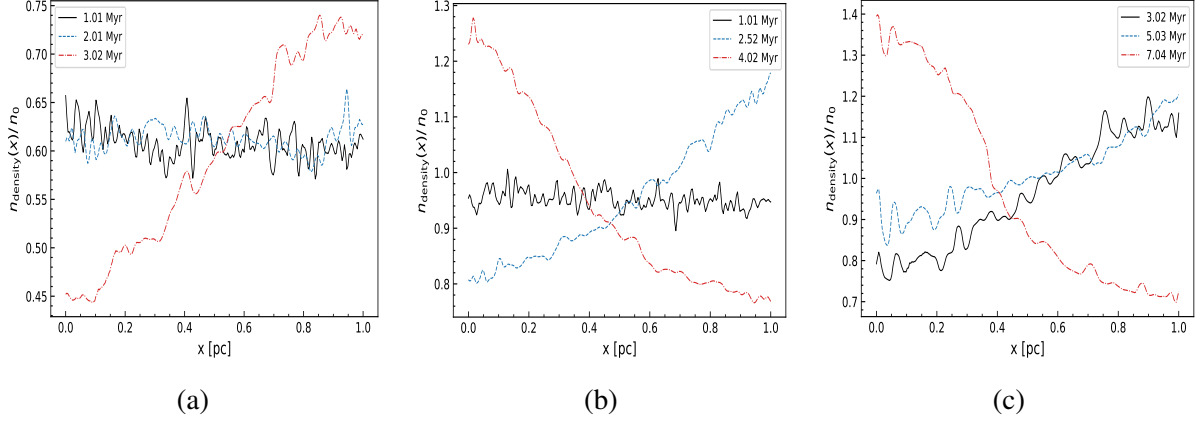


Figure 4.9: Number density plot normalized by the mean number density (n_0) for perpendicular cuts at the midplane ($y = 0.5$ pc) for different timesteps. The plots show models with a medium magnetic field strength, but for different density profiles. (a) High-gravity stratified field, (b) low-gravity stratified field, and (c) uniform density field.

683 mum density contrast observed for the perpendicular cut at the midplane is around 14% for the
 684 density field under high-gravity. This is significantly lower than the 30% density contrast esti-
 685 mated for the same density profile but with medium magnetic field strength. The low gravity
 686 stratified density field, shown in Figure 4.10(b), experiences very weak compressions with the
 687 maximum contrast close to 9% and indicates that both the weak Alfvén waves and compressive
 688 fast magnetosonic modes lost most of their energy and were largely dissipated. Similarly, even
 689 after 7 Myrs of continuous influx of Alfvén waves and evolution, the uniform density field does
 690 not experience strong compression as seen in Figure 4.10(c).

691

692 In the strong magnetic field models, the cloud experiences high-amplitude Alfvén waves
 693 ($\delta B/B \simeq 0.1$). Efficient phase-mixing caused by higher-amplitude Alfvén waves and den-
 694 sity stratification leads to more magnetic energy dissipated as fast magnetosonic compressive
 695 waves than in weaker magnetic fields. As observed in the Figure 4.11(a), although we ex-
 696 pected stronger compression, the maximum density contrast at the midplane is around 19%,
 697 which is still lower than the contrast estimated for the medium magnetic field case. This is be-
 698 cause the fast-magnetosonic waves do not generate a sufficient magnetic pressure gradient that
 699 forces strong background magnetic field lines to be pushed closer to the boundaries. Therefore,
 700 weaker compression fingerprints are observed in the normalized number density plots for both
 701 the low-gravity stratified density field, as shown in Figure 4.11(b) and the uniform density field
 702 shown in Figure 4.11(c).

703

704 To efficiently compare the structural changes observed with different magnetic field strengths
 705 across all the models, we plot the maximum density contrast in the number density plots against
 706 the ratio of Alfvén to isothermal sound speed (v_A/c_s), which maps magnetic field strength in
 707 Figure 4.12. Higher values of v_A/c_s indicate stronger magnetic fields because we assumed simi-
 708 lar isothermal conditions across all models. As we increase B_0 , v_A on average increases across
 709 all density profiles. To calculate the maximum density contrast, we first identify the two den-

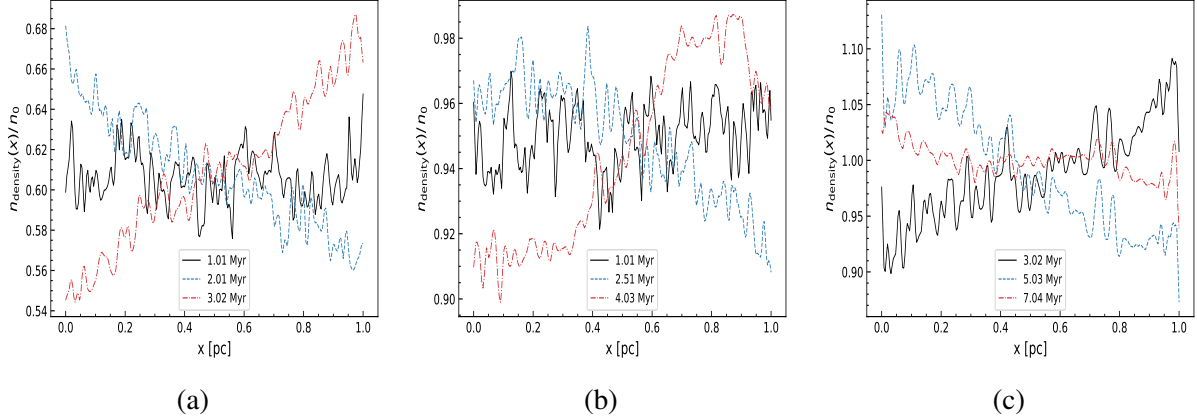


Figure 4.10: Normalized number density plot for perpendicular cuts at the midplane ($y = 0.5$ pc), for the weak magnetic field and different density profiles. (a) high-gravity stratified density field, (b) low-gravity stratified density field, and (c) uniform density field.

sity extremes that map the compressed and rarefied regions in the cloud along perpendicular cuts at different heights. Furthermore, the maximum contrast at different heights is calculated and averaged out to get a maximum contrast for the cloud. To improve the signal-to-noise ratio, we first average the number density and B_y over three adjacent lines neighbouring a perpendicular cut, then compute the maximum contrast by identifying the two extrema. In Figure 4.12, we observe that all the different density profiles with magnetic fields (v_A/c_s) between 2 and 4 achieve the highest number density contrast. Weakest magnetic field does not experience efficient coupling because Alfvén waves have low amplitudes, and we expect that a major fraction of Alfvén waves' energy is lost to numerical effects rather than fast magnetosonic modes. This is consistent with the findings of Nakariakov and Oraevsky (1995) and Nakariakov et al. (1997). They pointed out that strength of fast magnetosonic modes depends on the amplitude of the Alfvén wave to which they are coupled.

722

We further examine the influence of compressive waves on the background magnetic field. We plot the maximum contrast in the y -component magnetic field B_y in Figure 4.12. We follow the same strategy for calculating the magnetic field contrast between the compressed and rarefied region, as we did for density contrast. As shown in Figure 4.13, the magnetic field strengths in the range of 2 to 4 for v_A/c_s have the highest contrast in B_y among all the magnetic field strengths. Again, we observe that low-amplitude Alfvén waves in the weak magnetic field models ($v_a/c_s \sim 1$) lose a large share of their energy due to numerical effects. For stronger magnetic fields, we observe that although fast magnetosonic modes are generated, their pressure is insufficient to cause significant magnetic compression parallel to the background magnetic fields, and the contrast for each model drops drastically.

733

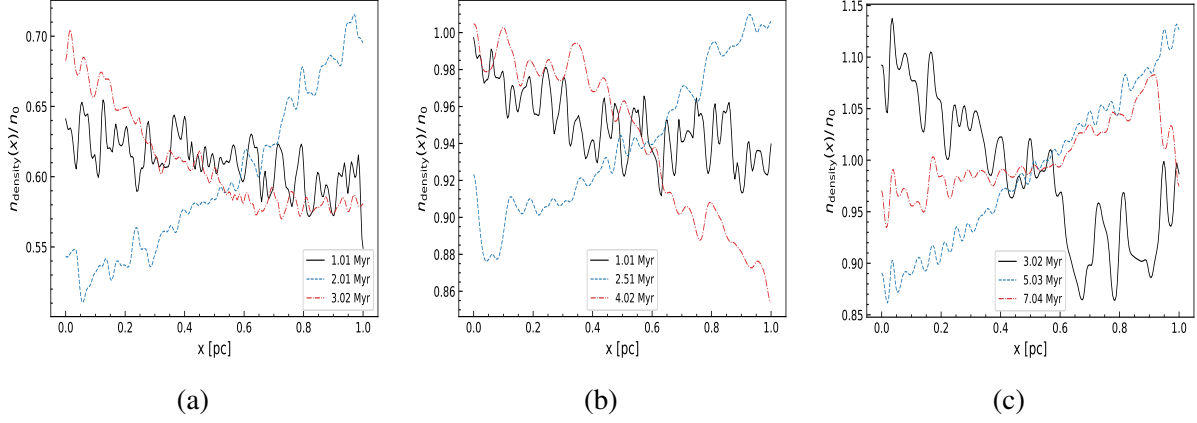


Figure 4.11: Similar to Figure 4.9 for models with strong magnetic fields. (a) High-gravity stratified density field, (b) low-gravity stratified density field, and (c) Uniform density field.

4.5 Evolution of MHD waves

Figures 4.7 to 4.13 provide strong evidence that input Alfvén waves are phase mixed and dissipate as compressive fast magnetosonic waves propagating perpendicular to the background magnetic field (have a v_x velocity component). To visualize how the power of the compressive waves redistributes across different spatial scales throughout the simulation timescale, we plot the number density power spectra in Figures 4.14, 4.15 and 4.16 for medium, weak and strong magnetic field strengths, respectively (at three different time steps: 0.34, 2.01 and 3.01 Myr). We compare the results for the high-gravity stratified density field.

During the initial stages of evolution for the medium magnetic field model, the profile at 0.34 Myr in Figure 4.14 shows a relatively flat power spectrum, and power is distributed uniformly across all scales, with peaks present at smaller spatial frequencies. This is because initially, phase mixing occurs uniformly throughout the cloud wherever a sharp density gradient exists due to the randomly perturbed density field. This is because the coupling of fast magnetosonic waves occurs at these random localized points that have the spatial resolution of the grid $\sim 7.8 \times 10^{-3}$ pc.

Eventually, the small-scale fast magnetosonic waves propagate, reflect from the boundaries along the x-direction, and interact with one another. These interactions form large-scale normal modes (Tritsis and Tassis, 2018), and the power is redistributed to larger scales (closer to the box width size L_x). We see this effect in the power spectra for the plot lines at 2 and 3 Myr in Figure 4.14, where the power at smaller spatial frequencies (box-level scale size) is remarkably higher than that at larger spatial frequencies (grid-level scale size). At 3 Myr, we observed a large-scale compressed region in the number density plot shown in Figure 4.9 of a perpendicular cut at the midplane. This compressed region accounts for most of the power and is supported by the peak in the power spectrum at the lowest spatial frequency at 3 Myr in Figure 4.14. For a weaker magnetic field strength, as we evolve in the simulation, the power increases at smaller spatial frequencies, similar to the medium magnetic field simulation, as

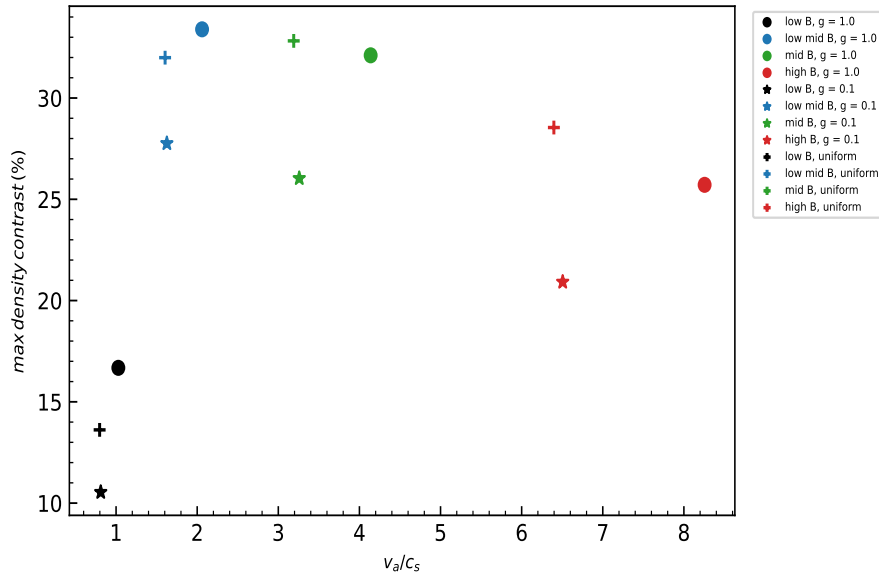


Figure 4.12: Maximum density contrast calculated by averaging out maximum contrasts from several perpendicular cuts to the background magnetic field. Molecular clouds with v_A/c_s in between 2 and 4 exhibit the maximum density contrast.

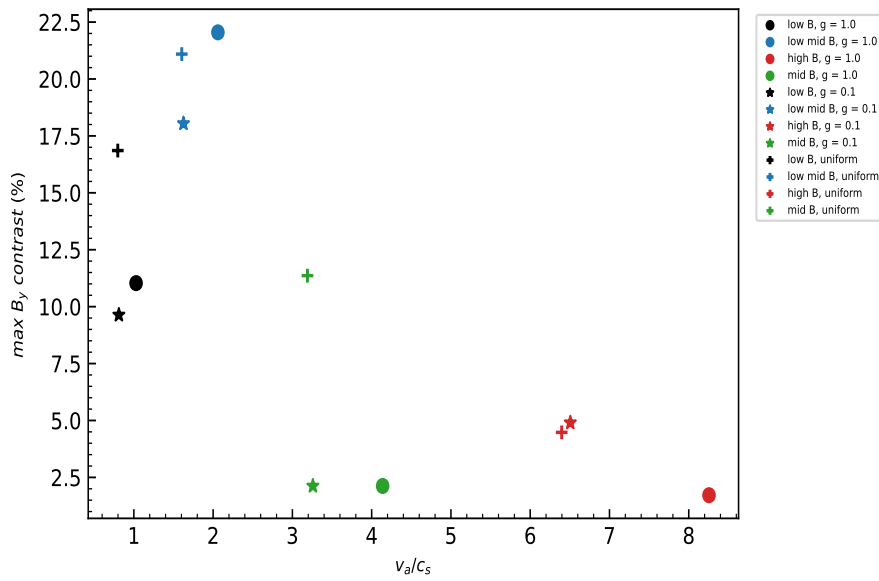


Figure 4.13: Maximum magnetic field B_y contrast calculated by averaging out maximum contrasts from several perpendicular cuts to the background magnetic field. Again, as we saw in Figure 4.12, Molecular clouds with v_A/c_s in between 2 and 4 experience maximum magnetic field contrast.

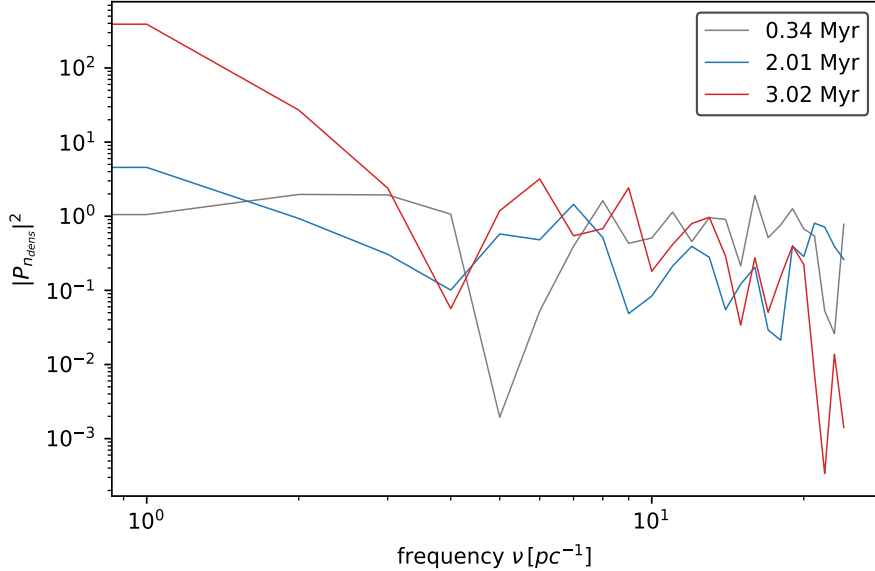


Figure 4.14: Power spectra for **medium** magnetic field and high-gravity stratified density model at three different time steps: 0.34, 2.01 and 3.02 Myr.

seen in Figure 4.15. Compared to the medium magnetic field power spectra, the magnitude of power for the weak magnetic field at small spatial frequencies is notably lower. Similarly, the power spectra shown in Figure 4.16 for the strong magnetic field exhibit a significant increase in power at lower spatial frequencies at 3 Myr. However, the peak power at each timestep is close to the medium magnetic field. Therefore, we expect that the peaks at smaller spatial frequencies in this case do not imply that compressive magnetosonic modes are strong enough to generate magnetic pressure and compress strong magnetic field lines.

We also expect redistribution of power to large-scale modes to be reflected in the evolution of physical properties of the cloud that should be instigated by large-scale compressive fast magnetosonic waves. Therefore, we plot the ratio of the magnitude of the net increase in the B_y , i.e. B'_y , to the B_x in Figure 4.17. The net increase in B'_y is defined as $B'_y = B_y - \bar{B}_y$, where \bar{B}_y is the average magnetic field's y-component. The ratio has been calculated at all grid points along cuts perpendicular to the background magnetic field, along the y-axis, at three different heights (0.25, 0.5 and 0.75 pc) and two time steps (0.34 and 2 Myr).

In Figure 4.17(a), at 0.34 Myr, we see that the ratio of B'_y to B_x is generally above one and highly fluctuating across the perpendicular cut. This is primarily because of the density white noise field added to the background uniform or stratified density fields. The white-noise random density fluctuations ensure effective phase-mixing at grid scales. The Alfvén waves couple and dissipate into fast magnetosonic waves at grid points with sharp density fluctuations (see Appendix A). The fast magnetosonic waves create small-scale pressure differences, compressing and expanding the gas locally, and increasing and decreasing the B_y component uniformly across the 2D box.

786

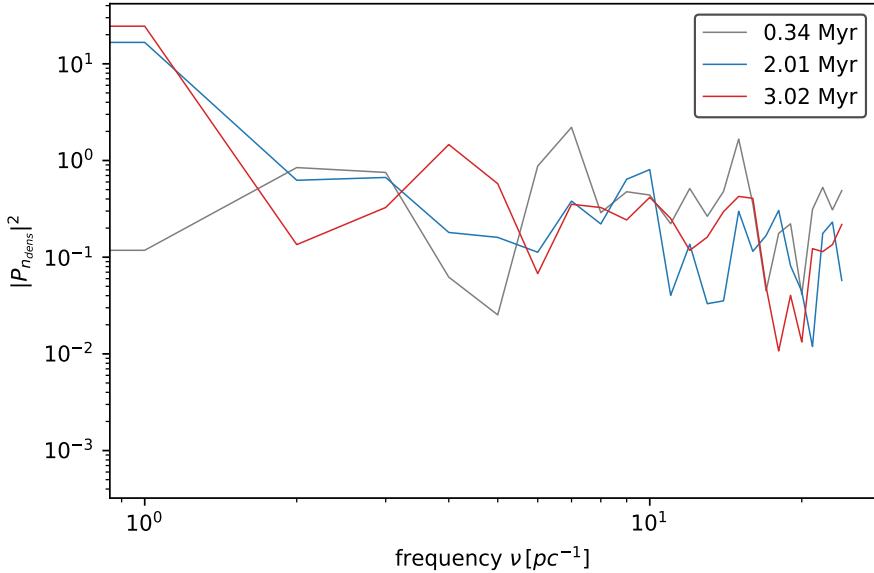


Figure 4.15: Power spectra for **low** magnetic field and high-gravity stratified density model at three different time steps: 0.34, 2.01 and 3.02 Myr.

In 4.17(b), we see a huge difference in the profile of the ratio of B'_y to B_x for the perpendicular cuts at the same heights as Figure 4.17(a). The cloud experiences the influence of large-scale compressions at 0.5 and 0.75 pc heights, resulting in high values of B'_y relative to B_x at most of the grid points along the perpendicular cut. We observe that some regions at $y = 0.5$ pc have a higher B_x component, and B'_y/B_x is less than 1. It is because the magnetosonic modes continuously reflect and propagate, and the regions around heights of 0.5 pc experience significant compression near the boundaries and are rarefied in between. This transformation from random small-scale effects to larger-scale trends supports the observations made from the number density power spectra shown in Figures 4.14 to 4.16, where initially, power is distributed uniformly across the 2D box mostly at smaller scales, but as the system evolves, wave interactions redistribute the power to higher scales and lower spatial frequencies.

We also observe a similar paradigm shift at larger scales in Figure 4.18, which plots the ratio of v_x to v_y velocity components at each grid point at the same heights as chosen for Figure 4.17. Equation A.2 (discussed in Appendix A) is the equation for the non-linear fast magnetosonic waves and describes that the transverse gradient in magnetic pressure ($B_y^2/8\pi$) and the velocity perpendicular to the magnetic field lines (v_x) are coupled with each other. Therefore, the magnetic pressure gradient generated by propagating magnetosonic waves exerts a force that pushes the medium to move perpendicular to the large-scale magnetic field.

In Figure 4.18, after 0.34 Myr, there exist only small-scale fluctuations for the ratio of velocity components at each grid point. The small-scale fluctuations transition into a large-scale trend as seen in Figure 4.18(b). Most regions at all three heights have v_x/v_y bigger than 1, meaning that the pressure gradient force is pushing the gas to move perpendicular to the striations and magnetic field rather than along the field lines. Because of the negative sign appearing

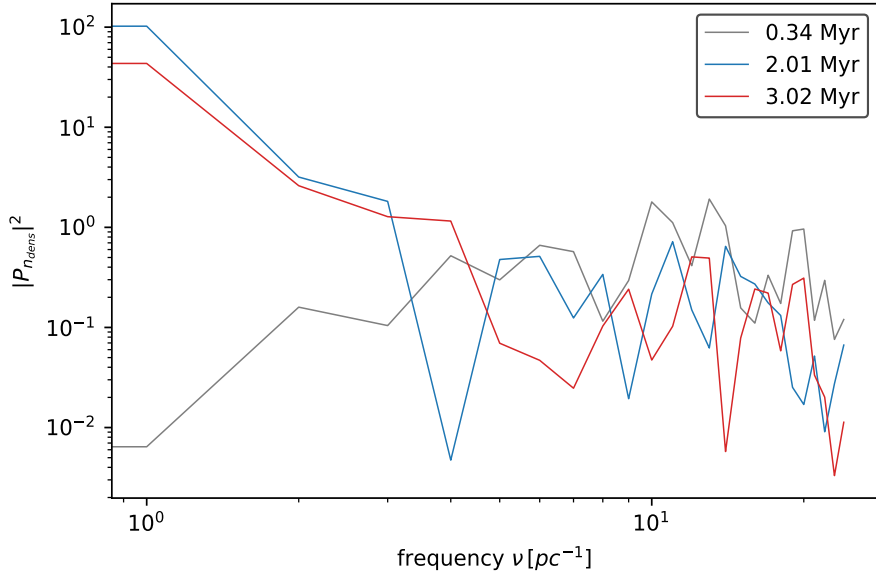


Figure 4.16: Power spectra for the **strong** magnetic field and high-gravity stratified density model at three different time steps: 0.34, 2.01 and 3.02 Myr.

812 in the Equation A.2, on both the smaller and larger scales, the trend seen in Figure 4.18(b) for
 813 the velocity components is somewhat opposite to the trend seen Figure 4.17(b) for the ratio
 814 of magnetic field components. We find that the trends observed in the physical properties on
 815 larger scales in v_x and B_y for our models are consistent with non-linear theoretical insights for
 816 the fast magnetosonic wave.
 817

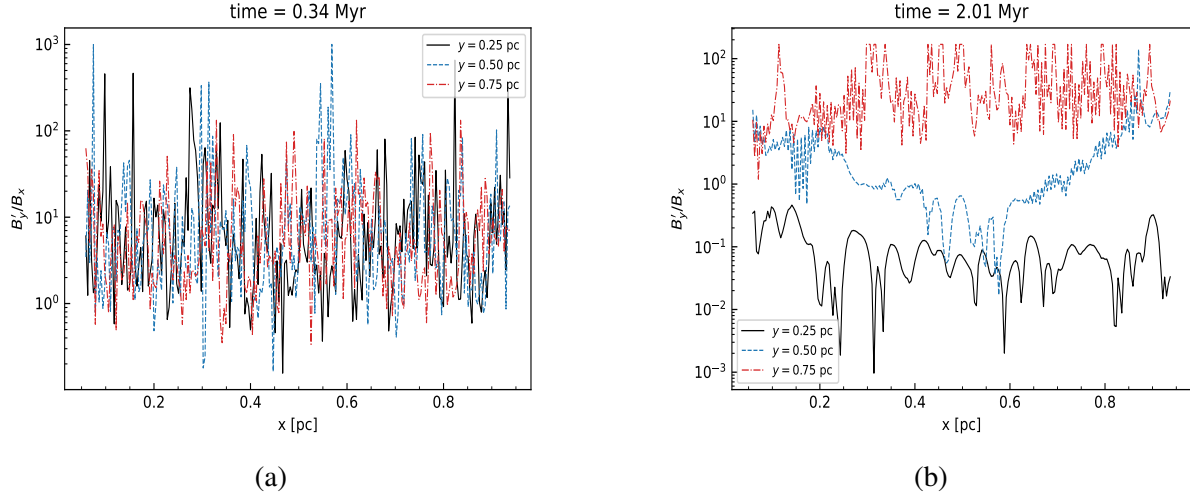


Figure 4.17: Ratio of B'_y ($B'_y = B_y - \bar{B}_y$) to B_x component of magnetic field for perpendicular cuts at heights of 0.25, 0.50 and 0.75 pc. (a) B'_y/B_x at 0.34 Myr. (b) B'_y/B_x at 2 Myr.

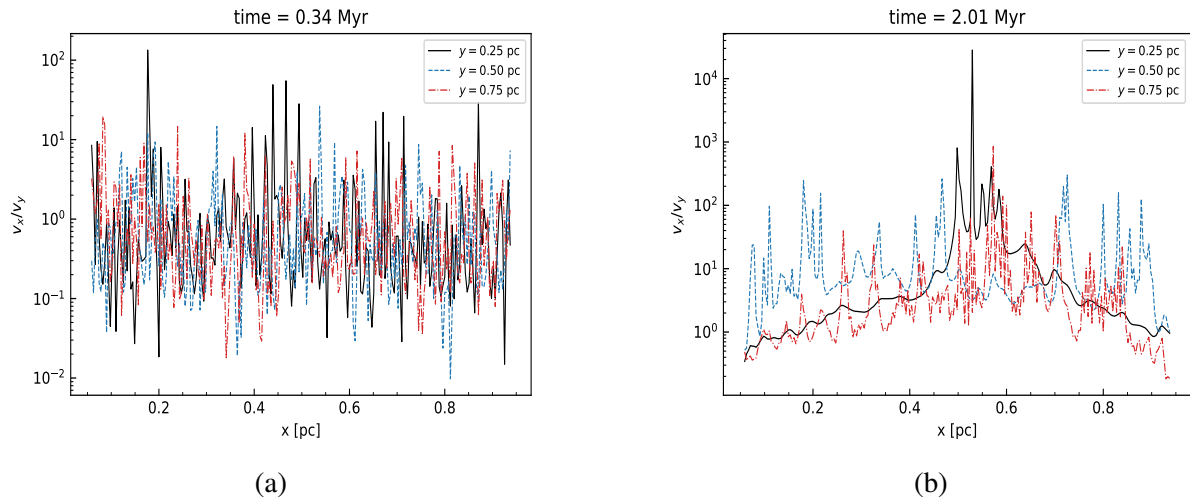


Figure 4.18: Ratio of the v_x to v_y velocity component for perpendicular cuts at height of 0.25, 0.50 and 0.75 pc. (a) v_x/v_y at 0.34 Myr. (b) v_x/v_y at 2 Myr.

818

Chapter 5

819

Discussion

820 MHD waves are ubiquitous in molecular clouds, and their influence on the structural and physical properties of the gas within the clouds remains largely unexplored, making this a potential
821 area of research. The discovery of elongated structures well-aligned with the plane-of-sky magnetic
822 field B_{pos} in the Taurus molecular cloud, termed ‘striations’ by Goldsmith et al. (2008),
823 provided a strong initial evidence that magnetically driven systems are influenced by magnetic
824 perturbations such as MHD waves. Striations revealed the first imprints of MHD waves due
825 to their quasiperiodic, anisotropic and well-ordered nature, which is unlikely to be caused by
826 turbulent interactions. It was not until numerical simulations by Tritsis and Tassis (2016) that
827 MHD waves were considered the main mechanism for the formation of striations. By per-
828 forming several 2D and 3D ideal MHD simulations, they found conclusive evidence that only
829 compressive MHD waves create quasiperiodic striations with physical properties similar to the
830 striations seen in the Taurus Molecular Cloud.

832

833 Following the pioneering research conducted by Tritsis and Tassis (2016), several studies
834 Heyer et al. (2016); Sun et al. (2024); Tritsis et al. (2018); Tritsis and Tassis (2018); Skalidis
835 et al. (2023); Skalidis et al. (2025) also reported that MHD waves, particularly fast magneto-
836 sonic waves, can explain the formation mechanism of striations and their observed periodic-
837 ity, elongated and well-aligned structure, and dynamic timescales. However, there is still much
838 to explore through numerical simulations to understand the complete picture of the formation
839 evolution of striations by fast magnetosonic waves. The ideal MHD simulations run by Trit-
840 sis and Tassis (2016) and Tritsis et al. (2018) present a secluded picture. The models did not
841 consider the chaotic nature of molecular clouds and the presence of denser structures near the
842 roots of striations.

843

844 Most of the molecular clouds where striations have been observed exhibit high star-forming
845 activities in the denser filaments to which they are connected. These star-forming cores are
846 known to send magnetic disturbances into the outer regions of their host molecular clouds
847 through feedback as strong winds, outflows and jets. The star-forming activity has been esti-
848 mated to last for a maximum of a few Myrs, and the lifetimes of filamentary structures have
849 been predicted to be less than 10 Myr (Kumar et al., 2020). Several studies have pointed out
850 that flows along striations can shape the growth and evolution of the dense structure and set the
851 initial conditions for active star formation. These denser structures also gravitationally influ-

ence striations due to their significantly greater mass and would create stratified atmospheric conditions, assuming hydrostatic balance. The influence of magnetic disturbances arising from star formation and gravity imposed by the denser structures has not previously been explored in the ideal MHD simulations (Tritsis and Tassis, 2016; Tritsis et al., 2018).

In this study, we incorporate both physical factors that were previously overlooked. We run 2D ideal MHD simulations using ATHENA++ and introduce two new conditions: (i) a continuous source of Alfvén waves and (ii) a constant gravitational field creating a stratified density field along the y-axis. Inspired by the properties of the outer regions discussed by Goldsmith et al. (2008) and Chapman et al. (2011), and also used in the MHD models by Tritsis and Tassis (2016), we choose similar initial thermal and physical conditions for our 2D models. We run and compare simulations for three different density profiles: (i) uniform density field, (ii) stratified density field under low-gravity and (iii) stratified density field under high-gravity. The new boundary conditions ensure that the cloud is in hydrostatic balance and has an exponentially varying stratified density profile with no mass loss occurring due to the gravitational field. For each model, we ran simulations for four magnetic field strengths, inspired by plane-of-sky magnetic field (B_{pos}) estimates for the Taurus, Musca, and L914 molecular clouds. Through newly designed 2D MHD simulations, we performed a comprehensive study on the formation and evolution of striations in different physical conditions and magnetic field strengths.

Firstly, we ran 2D ideal MHD simulations for a cloud with a uniform density field. Similar to the results obtained by Tritsis and Tassis (2016), for the uniform-density field coupled with random density perturbations, we find elongated striations forming in the cloud. These striations take 3 to 4 Myr to completely form and maintain their structural properties for around ~ 10 Myr. With a source of Alfvén waves perturbing the cloud, we find that the striations achieve a mean density contrast of approximately $\sim 11\%$ and a maximum density contrast of $\sim 32\%$. Tritsis and Tassis (2016) also found that perturbing the cloud with a spectrum of Alfvén waves resulted in a mean density contrasts of 7 %.

From Figures 4.9 to 4.13, we do see that large-scale magnetosonic modes have appeared in the simulations involving a uniform density field; however, we don't observe the aftereffects of pressure enforced by compressive fast magnetosonic waves that should change the structural scales and shape of striations and should induce a flow perpendicular to the background magnetic field. The number density slice maps for the uniform density field seen in Figure 4.1 show that fast-magnetosonic waves do propagate and compress regions parallel to the background magnetic field, but striations rarely transform further after 3 Myr.

Observations made for the Taurus molecular cloud by Goldsmith et al. (2008) and Heyer et al. (2016) show that striations exist on smaller scales. Recent observations performed by Skalidis et al. (2023) estimated the physical properties of striations in certain regions of Polaris Flare, and Sun et al. (2024) studied striations observed in the L914 molecular cloud. These studies revealed quasiperiodic density compressions that appear as striations on much larger scales than in the early studies by Goldsmith et al. (2008) and Heyer et al. (2016). In these studies periodicity of striations is estimated to lie in the range of 0.5 to 1.5 pc for both Polaris Flare and L914. Therefore, the uniform density field simulations fall short in explaining how

897 the striations evolve from small-scale, densely packed structures to large-scale, highly elongated
898 quasi-periodic patterns.

899
900 Furthermore, we performed 2D ideal MHD simulations on ATHENA++ for a stratified den-
901 sity field under a weaker gravitational field. As shown in Figure 4.3, striations form and evolve
902 at different scales throughout the entire evolution. This phenomenon has not been observed in
903 simulations performed with an initially uniform density field and no gravity (Tritsis and Tassis,
904 2016; Tritsis et al., 2018). Striations form at smaller scales after around \sim 1 Myr, much earlier
905 than the uniform density field. The small-scale striations initially form due to compressions in-
906 duced by localized coupling of Alfvén and compressive fast magnetosonic waves. The scales
907 of these compressions are similar to the initial white noise density perturbations and thus ap-
908 pear isotropic and densely packed.

909
910 We find that as we increase the magnetic field strength, the conditions for non-linear
911 coupling of MHD waves become more favourable, due to higher-amplitude Alfvén waves
912 and higher Alfvén speeds. These conditions ensure efficient phase-mixing and coupling of
913 Alfvén wave perturbations with compressive fast magnetosonic waves, which are in good
914 agreement with the theoretical findings of Nakariakov et al. (1997) and the insights we dis-
915 cuss in detail in Appendix A for our 2D model. Compressive magnetosonic waves propagate
916 and reflect from the reflective boundaries of the 2D box, gradually forming large-scale mag-
917 netosonic modes. Tritsis and Tassis (2018) confirmed the existence of magnetosonic normal
918 modes in the Musca molecular cloud and provided the first evidence of the propagating MHD
919 waves and their influence on the low-density regions. Through the normal mode analysis, they
920 estimated the dimensions of the Musca molecular cloud and found that it has a more sheet-like
921 dense structure. Magnetic pressure gradient generated by large-scale fast magnetosonic modes
922 compresses and pushes the medium, forming a region of higher density and highly elongated
923 striations as seen in the second and third rows of Figure 4.3. The transformation of small-scale
924 density compressions into large-scale structures is observed in numerical simulations when
925 gravitational influence is included and has not been observed before.

926
927 Lastly, we explored the evolution of striations in a strong gravitational field, creating a
928 stratified atmosphere. We use the same physical conditions and magnetic field strengths as in
929 previous models, but we modify the density profile to maintain a hydrostatic balance, thereby
930 counteracting stronger gravity. The number density slice maps in the first row of Figure 4.5
931 show that small-scale striations in the cloud with a weak magnetic field after 1 Myr. These
932 small-scale striations do not evolve any further, unlike previous models. Striations again
933 form isotropically due to the localized dissipation of fast magnetosonic waves caused by a
934 random density field. Due to a strong density contrast in the y-direction, we anticipate that
935 low-amplitude Alfvén waves perturbed into the system from the boundary at $y = 0$ pc lose sig-
936 nificant energy in the high-density regions closer to the boundary. Thus, the cloud persists with
937 small-scale striations densely packed for the entire timescale. Striations at smaller scales have
938 been observed in both Taurus (Goldsmith et al., 2008; Heyer et al., 2016) and Musca molecular
939 clouds.

940
941 As we increased the magnetic field strength and injected higher-amplitude Alfvén pertur-

bations, the cloud transitioned from small-scale striations at 1 Myr to elongated striations at 3 Myr, which were largely confined to the compressed regions. Compared to all the other models, the model with medium magnetic field achieved the highest maximum density contrast (34 %) and magnetic-field pressure compression (21 %). Over the full velocity interval, Skalidis et al. (2025) found that the surface brightness increments of striations are 15-25 % above the background CO total emission. Also, Sun et al. (2024) estimated that the density contrast on and off the striation in L914 is between 12% to 28%. This is in good agreement with our models with a stratified density profile and medium to high magnetic field strengths, where compressed regions representing striations and rarefied regions representing background medium have density contrasts of 15-35 %. The strongest magnetic field also experiences the influence of fast magnetosonic waves. However, the magnetic pressure $B_y^2/8\pi$ induced by fast magnetosonic modes is less efficient in pushing and compressing the strong background magnetic field lines. This results in a slight decrease in maximum density contrast and magnetic compression. This can be observed as an initially increasing trend as we increase magnetic field strength, followed by a decreasing trend in Figure 4.12 and 4.13 as we approach powerful magnetic fields.

The number density power spectra ($P_{n_{\text{dens}}}$) shown in Figures 4.14 to 4.15 illustrate how power is redistributed from smaller to large scales as the cloud continues to evolve. After 0.34 Myr of evolution, the power spectrum profile is relatively flat, with peaks at higher spatial frequencies, indicating that relatively more power is stored at smaller scales. This flat power-spectrum trend is consistent across all the magnetic field strengths. After 2 Myr, the dominant peaks are at lower spatial frequencies, indicating that large-scale fast magnetosonic waves have appeared. These peaks are in excellent agreement with the power spectrum analysis by Tritsis and Tassis (2016); Tritsis et al. (2018); Tritsis and Tassis (2018); Sun et al. (2024), which also found peaks at the lowest frequencies or wavenumber. In Figures 4.17 and 4.18, we again observe that after 0.34 Myr of evolution, the system undergoes physical changes at small scales that are consistent at all different heights. As the cloud evolves under the constant influx of Alfvén waves, large-scale magnetosonic waves form approximately 2 Myr. These compressive waves gradually forms normal modes and transform the physical and dynamical properties of the cloud to show the large-scale effects as seen in both the y component of magnetic field (B_y) shown in Figure 4.17(b) and velocity perpendicular to the background field (v_x) observed in Figure 4.18(b).

We find that the large-scale compressed regions exhibit properties similar to those observed for striations in molecular clouds. For the models with ratio of Alfvén to isothermal sound speed v_A/c_s ranging from 2 to 4 (medium to high magnetic field strengths), we find that the density contrast between the compressed and rarefied regions in models with stratified atmospheres is in excellent agreement with the findings of intensity contrast done by Skalidis et al. (2023), Skalidis et al. (2025) and Sun et al. (2024). The periodicity of the compressed and rarefied regions in our models appears to be twice the box size along the x -direction ($2L_x$), equivalent to ~ 2 pc, which also matches the periodicity of striations observed in recent studies ranging from 0.5 to 1.5 pc. Although future work is required to understand the factors that decide the wavelength or periodicity of these large-scale magnetosonic modes, we expect that the box size along the x -axis and the frequency of source Alfvén wave perturbations could

be interplaying. We also find that the timescales for large-scale striations to form are around 2 – 4 Myrs for the models with stratified density field and higher magnetic field strengths. These timescales are well within the lifetimes of molecular clouds and their star-forming activity (André et al., 2014; Kumar et al., 2020). Also, these formation timescales agree with the dynamical times needed to form molecular gas in the outer diffuse regions (Skalidis et al., 2023). We conclude that our 2D simulations, run with ATHENA++ having stratified density fields and continuous influx of Alfvén waves, provide a broader and detailed picture of the influence of MHD waves on the outer diffuse regions of molecular clouds. Our results present strong evidence and support the fact that propagating compressive MHD waves are the mechanism behind the formation of elongated striations well aligned with the large-scale preserved magnetic fields.

998 **Chapter 6**

999 **Conclusion**

1000 We present 2D ideal MHD simulations of molecular clouds perturbed by a continuous influx
1001 of Alfvén disturbances. We further investigate the influence of a constant gravitational field
1002 and stratified density profile on the evolution of the cloud. We reveal that striations do form in
1003 all the models, but their structural properties and evolution vary with different initial physical
1004 conditions. One of the main takeaways is that gravitational influence does affect how striations
1005 form and evolve. The other key point is that the source of Alfvén waves ensures that the cloud
1006 is continuously disturbed with a spectrum of waves, and the magnetic energy is pumped into
1007 the system. The Alfvén waves dissipate and lose their energy as fast magnetosonic waves.

1008

1009 We find strong evidence that MHD waves are dynamically important and influence molecu-
1010 lar clouds on different scales. These waves originate in denser regions with high stellar activity
1011 and are pumped out into the low-density outer regions by stellar feedback such as winds, out-
1012 flows and jets. We find that MHD waves alter the structural and physical properties of the outer
1013 regions. The presence of sub-Alfvénic conditions in the outer regions, along with density fluc-
1014 tuations, causes the transversal MHD waves, the Alfvén waves, to phase mix. High-amplitude
1015 Alfvén waves propagate in strong magnetic-field environments, and density fluctuations seed
1016 a strong transverse gradient in Alfvén speed ($\partial v_A / \partial x$). These conditions enforce Alfvén waves
1017 to dissipate as fast magnetosonic waves.

1018

1019 Under the influence of gravity, which creates a stratified density field, we find that in the
1020 early stages, striations form at smaller scales uniformly throughout the cloud. Non-linear cou-
1021 pling of Alfvén and fast magnetosonic waves occurs at grid points where the density gradient is
1022 sharp. These grid points are randomly distributed across the grid. The compression produced
1023 by localized magnetosonic waves results in deviations in density, transverse velocity (v_x) and
1024 magnetic field (B_y) at smaller scales. We find evidence of peaks observed at higher spatial
1025 frequencies in the number density and velocity power spectra.

1026

1027 As not observed in simulations with a uniform density field, the striations in the new 2D
1028 models (under constant gravity) gradually evolve and transform. Because of the reflective
1029 boundary conditions, small-scale fast magnetosonic waves are trapped, and they continuously
1030 reflect and interact. After around ~ 1 to 2 Myrs, these waves form large-scale magnetosonic
1031 modes with wavelengths set by the width of the 2D box (L_x) and the frequency (ω) of the

source Alfvén perturbations. Again, this paradigm shift to large-scale modes is evident in the shift in the peaks of number density and velocity power spectra from higher spatial frequencies at early stages to lower spatial frequencies seen after 2 to 3 Myr in evolution. The 2D number density and magnetic field slice maps show that the large-scale compression creates high-density regions with elongated striations well-aligned with the magnetic field (B_{pos}).

1037

The strength of the background magnetic field is an important factor. We notice no significant structural changes in clouds with weak magnetic fields perturbed by small-amplitude Alfvén waves. In these conditions, Alfvén waves either flow out of the system or are dissipated due to numerical artifacts or sharp density gradients. As we increase the magnetic field strength, the non-linear coupling between Alfvén and magnetosonic waves becomes efficient. We observe large structural changes in the cloud due to the magnetic pressure gradient ($B_y^2/8\pi$) created by the fast magnetosonic waves, which gradually superimpose and form normal modes.

1045

The structural scales of striations observed in molecular clouds may provide hints on their evolutionary timescales and magnetic properties. Striations observed at smaller scales uniformly distributed in the outer regions of the clouds could indicate a weak background magnetic field and low star-forming activity if a dense structure is observed nearby. Small-scale striations could also be seen in molecular clouds that are in relatively early stages of evolution and where magnetic fields have recently become dynamically important.

1052

Molecular clouds where striations have been observed at larger scales convey a different picture. These clouds will have stronger magnetic fields preserved even in the outer regions, in combination with active star-forming activities. We find that the initial ratio of Alfvén speed to isothermal sound speed v_A/c_s between 2 to 4, corresponding to medium to strong magnetic field strengths, experienced the strongest density compressions. Simulations with the initial setup in this range also achieved the highest density contrasts, and the values are close to density contrasts estimated in recent observations of striations. Active star formation continuously sends out excess magnetic energy into the diffuse regions of the cloud in the form of Alfvén disturbances. Also, these molecular clouds may have been existing for longer timescales, allowing MHD waves to propagate and gradually influence the preserved magnetic field and the diffuse regions in forming quasi-periodic patterns well-aligned with the background field, known as striations.

1065 **Chapter 7**

1066 **Future Work**

1067 We further plan to extend the analysis performed in this study in 3D and will perform 3D
1068 ideal MHD simulations, with a similar setup that includes a source of Alfvén waves and a
1069 gravitational field. The 3D setups allow us to study how Alfvén waves travelling along the
1070 background magnetic fields will phase-mix and propagate fast magnetosonic waves in a direc-
1071 tion transverse to both the Alfvén waves and background magnetic field. 2D simulations gave
1072 us a deep insight into the growth and influence of non-linear MHD waves and the evolution
1073 of striations parallel to the magnetic field. But the effects of line-of-sky B_{los} magnetic field
1074 component and projected effects are left out in the 2D models. Studies have revealed that some
1075 regions with striations have a larger B_{los} component, which may not be well-aligned with the
1076 threading magnetic field, and only the striations projection along the plane-of-sky seems to
1077 align with the smaller B_{pos} component. These theories could only be tested in a full 3D picture.

1078 Extending this approach to 3D, we can also test how circularly polarized Alfvén waves
1079 would behave as they also get coupled with fast magnetosonic modes appearing as sausage
1080 modes (Skalidis et al., 2025). The imprints of the sausage pressure waves have been found in
1081 Polaris Flare. 3D simulations will allow us to create synthetic dust emission and polarization
1082 maps. Through these synthetic observations, we can calculate the column density along the
1083 line-of-sight and will be able to efficiently compare our findings with the several observations.
1084 Through the dust polarization synthetic maps, we will compare the structure and scales of stri-
1085 ations at different scales and their alignment with the B_{pos} magnetic field component.

1086 In our simulations with gravity, we find that dense structures indeed play an important role
1087 in the formation and evolution of striations. However, several studies have found a velocity
1088 gradient along the long axis of striations. Material flows along the striations parallel to the
1089 background field, which can dynamically change the dense filaments or sheets to which the
1090 striations are usually connected. We have not presented the evolution of flow along the stri-
1091 ations in our 2D models, and have kept it as a future exploratory work. We will see both
1092 theoretically and numerically how the influx of Alfvén waves, gravity and later magnetosonic
1093 modes influences the flow along striations (v_y in our current 2D models), and whether magnetic
1094 field strength plays a deciding role.

1095 Through an intensive and broad spectrum of both 2D and 3D ideal MHD simulations us-

ing ATHENA++, we aim to present a thorough picture of the mechanism and evolution of striations. In our future work, we aim to compare our findings with existing observations of striations in several nearby molecular clouds, including Taurus, Musca, and Polaris Flare, to name a few. Our current findings provide strong insights into the involvement of MHD waves in the outer-diffuse regions of molecular clouds and the influence of a gravitational field and hydromagnetic waves on the formation and evolution of striations. But a 3D extension of our current setup will allow us to test the impact of projection effects and provide the flexibility to test different kinds of MHD waves. Using our 3D results, we will efficiently compare them with existing observations of striations. Our results on a specific range of magnetic fields where striations efficiently form will help constrain the boundary conditions for the future numerical models that will explore filamentary structures and star-forming regions, and will also allow observers to better compare the alignment of magnetic fields and striations and the estimations of magnetic field strengths of the outer diffused regions of molecular clouds.

1112

¹¹¹³ Bibliography

- ¹¹¹⁴ Alves de Oliveira, C., Schneider, N., Merín, B., Prusti, T., Ribas, Á., Cox, N. L. J.,
¹¹¹⁵ Vavrek, R., Könyves, V., Arzoumanian, D., Puga, E., Pilbratt, G. L., Kóspál, Á., André,
¹¹¹⁶ P., Didelon, P., Men'shchikov, A., Royer, P., Waelkens, C., Bontemps, S., Winston,
¹¹¹⁷ E., and Spezzi, L. (2014). Herschel view of the large-scale structure in the $\text{JAS-TROBJ}_\odot\text{Chamaeleon}/\text{ASTROBJ}_\odot$ dark clouds. , 568:A98.
- ¹¹¹⁹ André, P., Di Francesco, J., Ward-Thompson, D., Inutsuka, S.-I., Pudritz, R. E., and Pineda,
¹¹²⁰ J. E. (2014). From Filamentary Networks to Dense Cores in Molecular Clouds: Toward a
¹¹²¹ New Paradigm for Star Formation. In Beuther, H., Klessen, R. S., Dullemond, C. P., and
¹¹²² Henning, T., editors, *Protostars and Planets VI*, pages 27–51.
- ¹¹²³ Auddy, S., Basu, S., and Kudoh, T. (2016). A Magnetic Ribbon Model for Star-forming
¹¹²⁴ Filaments. , 831(1):46.
- ¹¹²⁵ Beattie, J. R. and Federrath, C. (2020). Filaments and striations: anisotropies in observed,
¹¹²⁶ supersonic, highly magnetized turbulent clouds. , 492(1):668–685.
- ¹¹²⁷ Chandrasekhar, S. and Fermi, E. (1953). Magnetic Fields in Spiral Arms. , 118:113.
- ¹¹²⁸ Chapman, N. L., Goldsmith, P. F., Pineda, J. L., Clemens, D. P., Li, D., and Krčo, M. (2011).
¹¹²⁹ The Magnetic Field in Taurus Probed by Infrared Polarization. , 741(1):21.
- ¹¹³⁰ Chen, C.-Y., Li, Z.-Y., King, P. K., and Fissel, L. M. (2017). Fantastic Striations and Where
¹¹³¹ to Find Them: The Origin of Magnetically Aligned Striations in Interstellar Clouds. ,
¹¹³² 847(2):140.
- ¹¹³³ Cox, N. L. J., Arzoumanian, D., André, P., Rygl, K. L. J., Prusti, T., Men'shchikov, A., Royer,
¹¹³⁴ P., Kóspál, Á., Palmeirim, P., Ribas, A., Könyves, V., Bernard, J.-P., Schneider, N., Bon-
¹¹³⁵ temps, S., Merin, B., Vavrek, R., Alves de Oliveira, C., Didelon, P., Pilbratt, G. L., and
¹¹³⁶ Waelkens, C. (2016). Filamentary structure and magnetic field orientation in Musca. ,
¹¹³⁷ 590:A110.
- ¹¹³⁸ Davis, L. (1951). The Strength of Interstellar Magnetic Fields. *Physical Review*, 81(5):890–
¹¹³⁹ 891.
- ¹¹⁴⁰ Federrath, C. and Klessen, R. S. (2012). The Star Formation Rate of Turbulent Magnetized
¹¹⁴¹ Clouds: Comparing Theory, Simulations, and Observations. , 761(2):156.

- 1142 Federrath, C., Rathborne, J. M., Longmore, S. N., Kruijssen, J. M. D., Bally, J., Contreras,
1143 Y., Crocker, R. M., Garay, G., Jackson, J. M., Testi, L., and Walsh, A. J. (2016). The
1144 Link between Turbulence, Magnetic Fields, Filaments, and Star Formation in the Central
1145 Molecular Zone Cloud G0.253+0.016. , 832(2):143.
- 1146 Goldsmith, P. F., Heyer, M., Narayanan, G., Snell, R., Li, D., and Brunt, C. (2008). Large-scale
1147 structure of the molecular gas in taurus revealed by high linear dynamic range spectral line
1148 mapping. *The Astrophysical Journal*, 680(1):428.
- 1149 Heyer, M., Goldsmith, P. F., Yıldız, U. A., Snell, R. L., Falgarone, E., and Pineda, J. L.
1150 (2016). Striations in the taurus molecular cloud: Kelvin–helmholtz instability or mhd waves?
1151 *Monthly Notices of the Royal Astronomical Society*, 461(4):3918–3926.
- 1152 Kudoh, T. and Basu, S. (2003). Nonlinear hydromagnetic wave support of a stratified molecular
1153 cloud. *The Astrophysical Journal*, 595(2):842.
- 1154 Kumar, M. S. N., Palmeirim, P., Arzoumanian, D., and Inutsuka, S. I. (2020). Unifying low-
1155 and high-mass star formation through density-amplified hubs of filaments. The highest mass
1156 stars ($> 100 M_{\odot}$) form only in hubs. , 642:A87.
- 1157 Malinen, J., Montier, L., Montillaud, J., Juvela, M., Ristorcelli, I., Clark, S. E., Berné, O.,
1158 Bernard, J.-P., Pelkonen, V.-M., and Collins, D. C. (2016). Matching dust emission struc-
1159 tures and magnetic field in high-latitude cloud 11642: comparing herschel and planck maps.
1160 *Monthly Notices of the Royal Astronomical Society*, 460(2):1934–1945.
- 1161 McKee, C. F. and Ostriker, E. C. (2007). Theory of Star Formation. , 45(1):565–687.
- 1162 Miville-Deschénes, M.-A., Martin, P. G., Abergel, A., Bernard, J.-P., Boulanger, F., Lagache,
1163 G., Anderson, L. D., André, P., Arab, H., Baluteau, J.-P., Blagrave, K., Bontemps, S., Cohen,
1164 M., Compiègne, M., Cox, P., Dartois, E., Davis, G., Emery, R., Fulton, T., Gry, C., Habart,
1165 E., Huang, M., Joblin, C., Jones, S. C., Kirk, J., Lim, T., Madden, S., Makiwa, G., Men-
1166 shchikov, A., Molinari, S., Moseley, H., Motte, F., Naylor, D. A., Okumura, K., Pinheiro
1167 Gonçalves, D., Polehampton, E., Rodón, J. A., Russeil, D., Saraceno, P., Schneider, N.,
1168 Sidher, S., Spencer, L., Swinyard, B., Ward-Thompson, D., White, G. J., and Zavagno, A.
1169 (2010). Herschel-SPIRE observations of the Polaris flare: Structure of the diffuse interstellar
1170 medium at the sub-parsec scale. , 518:L104.
- 1171 Molinari, S., Swinyard, B., Bally, J., Barlow, M., Bernard, J.-P., Martin, P., Moore, T., Noriega-
1172 Crespo, A., Plume, R., Testi, L., Zavagno, A., Abergel, A., Ali, B., Anderson, L., André,
1173 P., Baluteau, J.-P., Battersby, C., Beltrán, M. T., Benedettini, M., Billot, N., Blommaert,
1174 J., Bontemps, S., Boulanger, F., Brand, J., Brunt, C., Burton, M., Calzetti, L., Carey, S.,
1175 Caselli, P., Cesaroni, R., Cernicharo, J., Chakrabarti, S., Chrysostomou, A., Cohen, M.,
1176 Compiègne, M., de Bernardis, P., de Gasperis, G., di Giorgio, A. M., Elia, D., Faustini,
1177 F., Flagey, N., Fukui, Y., Fuller, G. A., Ganga, K., Garcia-Lario, P., Glenn, J., Goldsmith,
1178 P. F., Griffin, M., Hoare, M., Huang, M., Ikeno, D., Joblin, C., Joncas, G., Juvela, M.,
1179 Kirk, J. M., Lagache, G., Li, J. Z., Lim, T. L., Lord, S. D., Marengo, M., Marshall, D. J.,
1180 Masi, S., Massi, F., Matsuura, M., Minier, V., Miville-Deschénes, M.-A., Montier, L. A.,

- 1181 Morgan, L., Motte, F., Mottram, J. C., Müller, T. G., Natoli, P., Neves, J., Olmi, L., Paladini,
1182 R., Paradis, D., Parsons, H., Peretto, N., Pestalozzi, M., Pezzuto, S., Piacentini, F., Piazzo,
1183 L., Polychroni, D., Pomarès, M., Popescu, C. C., Reach, W. T., Ristorcelli, I., Robitaille,
1184 J.-F., Robitaille, T., Rodón, J. A., Roy, A., Royer, P., Russeil, D., Saraceno, P., Sauvage,
1185 M., Schilke, P., Schisano, E., Schneider, N., Schuller, F., Schulz, B., Sibthorpe, B., Smith,
1186 H. A., Smith, M. D., Spinoglio, L., Stamatellos, D., Strafella, F., Stringfellow, G. S., Sturm,
1187 E., Taylor, R., Thompson, M. A., Traficante, A., Tuffs, R. J., Umana, G., Valenziano, L.,
1188 Vavrek, R., Veneziani, M., Viti, S., Waelkens, C., Ward-Thompson, D., White, G., Wilcock,
1189 L. A., Wyrowski, F., Yorke, H. W., and Zhang, Q. (2010). Clouds, filaments, and protostars:
1190 The Herschel Hi-GAL Milky Way. , 518:L100.
- 1191 Nakariakov, V., Roberts, B., and Murawski, K. (1997). Alfvén wave phase mixing as a source
1192 of fast magnetosonic waves. *Solar Physics*, 175:93–105.
- 1193 Nakariakov, V. M. and Oraevsky, V. N. (1995). Resonant interactions of modes in coronal
1194 magnetic flux tubes. , 160(2):289–302.
- 1195 Orkisz, Jan H., Pety, Jérôme, Gerin, Maryvonne, Bron, Emeric, Guzmán, Viviana V., Bardeau,
1196 Sébastien, Goicoechea, Javier R., Gratier, Pierre, Le Petit, Franck, Levrier, François, Liszt,
1197 Harvey, Öberg, Karin, Peretto, Nicolas, Roueff, Evelyne, Sievers, Albrecht, and Tremblin,
1198 Pascal (2017). Turbulence and star formation efficiency in molecular clouds: solenoidal
1199 versus compressive motions in orionb. *AA*, 599:A99.
- 1200 Padoan, P., Federrath, C., Chabrier, G., Evans, II, N. J., Johnstone, D., Jørgensen, J. K., McKee,
1201 C. F., and Nordlund, Å. (2014). The Star Formation Rate of Molecular Clouds. In Beuther,
1202 H., Klessen, R. S., Dullemond, C. P., and Henning, T., editors, *Protostars and Planets VI*,
1203 pages 77–100.
- 1204 Palmeirim, P., André, P., Kirk, J., Ward-Thompson, D., Arzoumanian, D., Könyves, V., Dide-
1205 lon, P., Schneider, N., Benedettini, M., Bontemps, S., Di Francesco, J., Elia, D., Griffin, M.,
1206 Hennemann, M., Hill, T., Martin, P. G., Men'shchikov, A., Molinari, S., Motte, F., Nguyen
1207 Luong, Q., Nutter, D., Peretto, N., Pezzuto, S., Roy, A., Rygl, K. L. J., Spinoglio, L., and
1208 White, G. L. (2013). Herschel view of the Taurus B211/3 filament and striations: evidence
1209 of filamentary growth? , 550:A38.
- 1210 Panopoulou, G. V., Psaradaki, I., and Tassis, K. (2016). The magnetic field and dust filaments
1211 in the polaris flare. *Monthly Notices of the Royal Astronomical Society*, 462(2):1517–1529.
- 1212 Parker, E. N. (1991). The Phase Mixing of Alfvén Waves, Coordinated Modes, and Coronal
1213 Heating. , 376:355.
- 1214 Planck Collaboration, Adam, R., Ade, P. A. R., Aghanim, N., Alves, M. I. R., Arnaud, M.,
1215 Arzoumanian, D., Ashdown, M., Aumont, J., Baccigalupi, C., Banday, A. J., Barreiro,
1216 R. B., Bartolo, N., Battaner, E., Benabed, K., Benoit-Lévy, A., Bernard, J.-P., Bersanelli, M.,
1217 Bielewicz, P., Bonaldi, A., Bonavera, L., Bond, J. R., Borrill, J., Bouchet, F. R., Boulanger,
1218 F., Bracco, A., Burigana, C., Butler, R. C., Calabrese, E., Cardoso, J.-F., Catalano, A.,
1219 Chamballu, A., Chiang, H. C., Christensen, P. R., Colombi, S., Colombo, L. P. L., Combet,

- 1220 C., Couchot, F., Crill, B. P., Curto, A., Cuttaia, F., Danese, L., Davies, R. D., Davis, R. J.,
 1221 de Bernardis, P., de Rosa, A., de Zotti, G., Delabrouille, J., Dickinson, C., Diego, J. M.,
 1222 Dole, H., Donzelli, S., Doré, O., Douspis, M., Ducout, A., Dupac, X., Efstathiou, G., Elsner,
 1223 F., Enßlin, T. A., Eriksen, H. K., Falgarone, E., Ferrière, K., Finelli, F., Forni, O., Frailis,
 1224 M., Fraisse, A. A., Franceschi, E., Frejsel, A., Galeotta, S., Galli, S., Ganga, K., Ghosh,
 1225 T., Giard, M., Gjerløw, E., González-Nuevo, J., Górski, K. M., Gregorio, A., Gruppuso,
 1226 A., Guillet, V., Hansen, F. K., Hanson, D., Harrison, D. L., Henrot-Versillé, S., Hernández-
 1227 Monteagudo, C., Herranz, D., Hildebrandt, S. R., Hivon, E., Hobson, M., Holmes, W. A.,
 1228 Hovest, W., Huffenberger, K. M., Hurier, G., Jaffe, A. H., Jaffe, T. R., Jones, W. C., Ju-
 1229 vela, M., Keihänen, E., Keskitalo, R., Kisner, T. S., Kneissl, R., Knoche, J., Kunz, M.,
 1230 Kurki-Suonio, H., Lagache, G., Lamarre, J.-M., Lasenby, A., Lattanzi, M., Lawrence, C. R.,
 1231 Leonardi, R., Levrier, F., Liguori, M., Lilje, P. B., Linden-Vørnle, M., López-Caniego, M.,
 1232 Lubin, P. M., Macías-Pérez, J. F., Maffei, B., Maino, D., Mandolesi, N., Maris, M., Mar-
 1233 shall, D. J., Martin, P. G., Martínez-González, E., Masi, S., Matarrese, S., Mazzotta, P.,
 1234 Melchiorri, A., Mendes, L., Mennella, A., Migliaccio, M., Miville-Deschénes, M.-A., Mon-
 1235 etti, A., Montier, L., Morgante, G., Mortlock, D., Munshi, D., Murphy, J. A., Naselsky, P.,
 1236 Natoli, P., Nørgaard-Nielsen, H. U., Noviello, F., Novikov, D., Novikov, I., Oppermann, N.,
 1237 Oxborow, C. A., Pagano, L., Pajot, F., Paoletti, D., Pasian, F., Perdereau, O., Perotto, L.,
 1238 Perrotta, F., Pettorino, V., Piacentini, F., Piat, M., Plaszczynski, S., Pointecouteau, E., Po-
 1239 lenta, G., Ponthieu, N., Popa, L., Pratt, G. W., Prunet, S., Puget, J.-L., Rachen, J. P., Reach,
 1240 W. T., Reinecke, M., Remazeilles, M., Renault, C., Ristorcelli, I., Rocha, G., Roudier, G.,
 1241 Rubiño-Martín, J. A., Rusholme, B., Sandri, M., Santos, D., Savini, G., Scott, D., Soler,
 1242 J. D., Spencer, L. D., Stolyarov, V., Sudiwala, R., Sunyaev, R., Sutton, D., Suur-Uski, A.-S.,
 1243 Sygnet, J.-F., Tauber, J. A., Terenzi, L., Toffolatti, L., Tomasi, M., Tristram, M., Tucci, M.,
 1244 Umana, G., Valenziano, L., Valiviita, J., Van Tent, B., Vielva, P., Villa, F., Wade, L. A.,
 1245 Wandelt, B. D., and Wehus, I. K. (2016). Planck intermediate results. XXXII. The relative
 1246 orientation between the magnetic field and structures traced by interstellar dust. , 586:A135.

 1247 Skalidis, R., Gkimisi, K., Tassis, K., Panopoulou, G., Pelgrims, V., Tritsis, A., and Goldsmith,
 1248 P. (2023). Co enhancement by magnetohydrodynamic waves. striations in the polaris flare.
 1249 *Astronomy & Astrophysics*, 673.

 1250 Skalidis, R. and Tassis, K. (2021). High-accuracy estimation of magnetic field strength in the
 1251 interstellar medium from dust polarization. , 647:A186.

 1252 Skalidis, R., Tassis, K., Tritsis, A., and Goldsmith, P. F. (2025). Investigating the role of mag-
 1253 netic fields in the formation and evolution of striations in interstellar clouds with the probe
 1254 far-infrared mission for astrophysics. *Journal of Astronomical Telescopes, Instruments, and*
 1255 *Systems*, 11:031617.

 1256 Stone, J. M., Tomida, K., White, C. J., and Felker, K. G. (2020). The athena adaptive mesh re-
 1257 finement framework: Design and magnetohydrodynamic solvers. *The Astrophysical Journal*
 1258 *Supplement Series*, 249(1):4.

 1259 Sun, L., Chen, X., Fang, M., Zhang, S., Gong, Y., Feng, J., Li, X., Yan, Q.-Z., and Yang, J.
 1260 (2024). Magnetically aligned striations in the 1914 filamentary cloud. *The Astronomical*
 1261 *Journal*, 167(4):176.

- 1262 Tritsis, A., Federrath, C., Schneider, N., and Tassis, K. (2018). A new method for probing
1263 magnetic field strengths from striations in the interstellar medium. *Monthly Notices of the*
1264 *Royal Astronomical Society*, 481(4):5275–5285.
- 1265 Tritsis, A. and Tassis, K. (2016). Striations in molecular clouds: streamers or mhd waves?
1266 *Monthly Notices of the Royal Astronomical Society*, 462(4):3602–3615.
- 1267 Tritsis, A. and Tassis, K. (2018). Magnetic seismology of interstellar gas clouds: Unveiling a
1268 hidden dimension. *Science*, 360(6389):635–638.
- 1269 Wang, P., Li, Z.-Y., Abel, T., and Nakamura, F. (2010). Outflow Feedback Regulated Massive
1270 Star Formation in Parsec-Scale Cluster-Forming Clumps. , 709(1):27–41.
- 1271 Xu, S., Ji, S., and Lazarian, A. (2019). On the Formation of Density Filaments in the Turbulent
1272 Interstellar Medium. , 878(2):157.
- 1273 Yuan, L., Yang, J., Du, F., Liu, X., Zhang, S., Lin, Z., Sun, J., Yan, Q.-Z., Ma, Y., Su, Y.,
1274 Sun, Y., and Zhou, X. (2021). A Morphological Classification of 18,190 Molecular Clouds
1275 Identified in ^{12}CO Data from the MWISP Survey. , 257(2):51.

Appendix A

Fast magnetosonic equation

From the large-scale and opposite trends seen in Figure 4.17 and 4.18, we find that v_x and B_y appear to be coupled. Nakariakov et al. (1997) derived the fast magnetosonic wave equation where transversal and temporal gradients in magnetic pressure enforce motion along the transversal direction non-linearly. Therefore, we follow the same approach as Nakariakov et al. (1997) to find the equation of fast magnetosonic wave for our 2D model.

Using the induction equations, Eq. 2.2 and Eq. 2.3 and the momentum equation in x-direction (transverse to magnetic field) Eq. 2.4, we derive a new equation A.1.

$$\begin{aligned} \frac{\partial B'_x}{\partial t} - B_0 \left(\frac{\partial v'_x}{\partial y} \right) &= N_2, \\ \frac{\partial B'_y}{\partial t} + B_0 \left(\frac{\partial v'_x}{\partial x} \right) &= N_3, \\ \rho_0 \frac{\partial v'_x}{\partial t} + \frac{B_0}{4\pi} \left(\frac{\partial B'_y}{\partial x} - \frac{\partial B'_x}{\partial y} \right) &= N_4, \\ \frac{\partial^2 v'_x}{\partial t^2} - v_A^2 \left(\frac{\partial^2 v'_x}{\partial x^2} + \frac{\partial^2 v'_x}{\partial y^2} \right) &= \frac{\partial N_4}{\rho_0 \partial t} - \frac{B_0}{4\pi} \frac{\partial N_3}{\partial x} + \frac{B_0}{4\pi} \frac{\partial N_2}{\partial y}. \end{aligned} \quad (\text{A.1})$$

N_2 , N_3 and N_4 , are the non-linear terms

$$\begin{aligned} N_2 &= \frac{\partial}{\partial y} (v'_x B'_y - v'_y B'_x), \\ N_3 &= -\frac{\partial}{\partial x} (v'_x B'_y - v'_y B'_x), \\ N_4 &= -\rho' \frac{\partial v'_x}{\partial t} - \frac{B'_y}{4\pi} \left[\frac{\partial B'_y}{\partial x} - \frac{\partial B'_x}{\partial y} \right]. \end{aligned}$$

1295 We further assume that only the transversal gradient (∂x) is significant and any higher-order
 1296 terms involving v'_x or v'_y can be neglected, since the medium is at rest initially. Therefore, the
 1297 only non-linear term that survives is N_4 , which is

$$N_4 = -\rho' \frac{\partial v'_x}{\partial t} - \frac{B'_y}{4\pi} \left[\frac{\partial B'_y}{\partial x} - \frac{\partial B'_x}{\partial y} \right],$$

1298
 1299 and applying the same assumptions, N_4 can be further simplified as

$$N_4 = -\frac{B'_y}{4\pi} \left[\frac{\partial B'_y}{\partial x} \right] = -\frac{\partial(\frac{B'_y}{8\pi})}{\partial x}.$$

1300
 1301 We use the simplified N_4 non-linear, the Eq. A.1 can be rearranged as

$$\frac{\partial^2 v'_x}{\partial t^2} - v_A^2 \left(\frac{\partial^2 v'_x}{\partial x^2} + \frac{\partial^2 v'_x}{\partial y^2} \right) = -\frac{1}{\rho_0} \left(\frac{\partial^2 (\frac{B'_y}{8\pi})}{\partial t \partial x} \right). \quad (\text{A.2})$$

1302
 1303 Eq. A.2 is the fast magnetosonic wave equation for the 2D model we considered. This equa-
 1304 tion shows that the temporal and transversal variations of magnetic pressure $B'_y/8\pi$ enforce
 1305 fast magnetosonic waves v_x through a non-linear coupling.

1306
 1307

1308 **Appendix B**

1309 **Convergence Test**

1310 In order to see if our simulation results converge, we ran the stratified medium under a strong
1311 gravitational field at two resolutions, 256^2 and 512^2 . In Figure B.1, we compare the power
1312 spectra for the medium magnetic field case at 2 Myr. We again find that at later stages of
1313 evolution, we see a peak in power spectra at smaller spatial frequencies for both resolutions,
1314 indicating that energy is stored at larger scales that define the cloud's structure and properties.

1315

1316 This trend is consistent at higher resolutions as well, where we see that for both the higher
1317 512^2 and lower 256^2 resolutions, the global peaks are at small spatial frequencies for both the
1318 number density and velocity fields. The power decreases as we move to larger spatial frequen-
1319 cies in both resolutions. Both resolutions also achieve a similar level of power, and local peaks
1320 at larger spatial frequencies closer to grid scales.

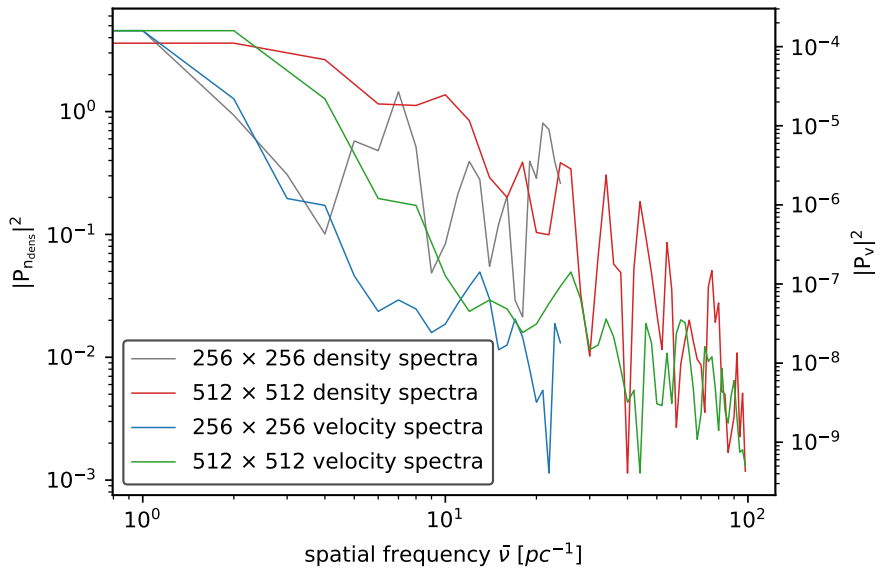


Figure B.1: Convergence test comparing the power spectra at 2 Myr for stratified medium with high gravity case with medium magnetic field strength at two resolutions, 256×256 and 512×512 . We find that the power spectra at two resolutions are in excellent agreement, with peaks at low spatial frequencies followed by a decreasing trend as we move to larger spatial frequencies.

¹³²¹ **Appendix C**

¹³²² **Magnetic Field Calculations**

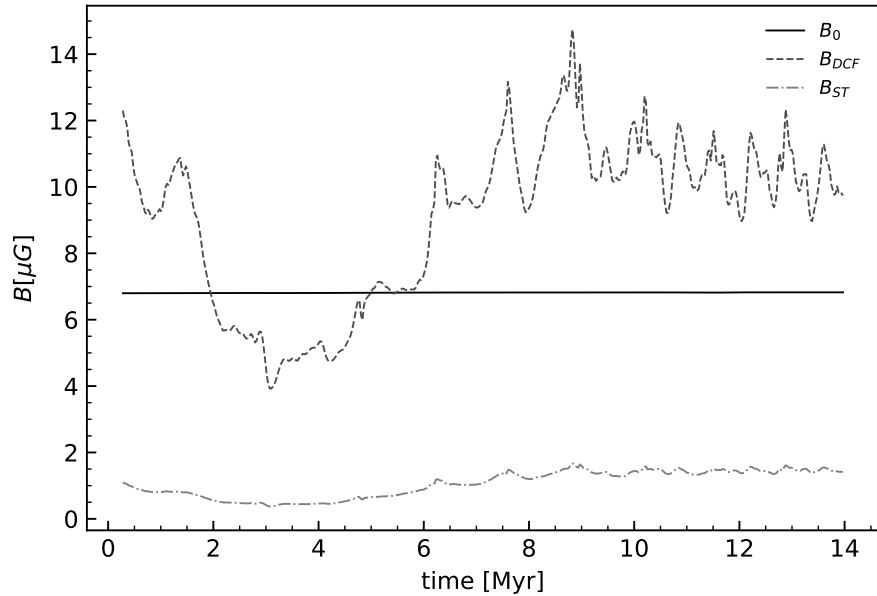


Figure C.1: Magnetic field estimations made using both the DCF and ST methods. The solid line shows the initial magnetic field in the simulation B_0 . The DCF method, on average, is closer to the actual value, while the ST method largely underestimates.

¹³²³ Figure C.1 compares the magnetic field computed in the simulations to the estimated magnetic field strengths using both the DCF (B_{DCF}) and ST (B_{ST}) methods for the medium magnetic field case. We used the following norms to calculate B_{DCF} and B_{ST}

$$B_{DCF} = Q \sqrt{4\pi\rho_0} \frac{\delta v}{\delta\theta},$$

$$B_{ST} = \sqrt{2\pi\rho_0} \frac{\delta v}{\sqrt{\delta\theta}},$$

¹³²⁶ where Q is the correction factor, assumed to be around 0.5. We calculate the velocity dispersion δv using the net velocity v , where $v = \sqrt{v_x^2 + v_y^2}$. For simplicity, we didn't apply the

1328 dust polarization schemes for the 2D results. We plan to do dust polarization analysis in a
1329 future study involving 3D simulations. Therefore, we utilized the magnetic field components
1330 B_x and B_y from our simulation datasets to compute the polarization angle θ at each grid point.
1331 In the end, we calculated the average polarization angle dispersion $\delta\theta$ and velocity dispersion
1332 δv for the whole grid at each timestep to calculate the magnetic field strength from the two
1333 approaches.

1334
1335 Estimates made by the DCF method on average agree with the true magnetic field strength,
1336 while the ST method largely underestimates. Compressive modes should decrease the polar-
1337 ization dispersion angle of magnetic fields, which is caused by the isotropic turbulence and in-
1338 compressible Alfvén waves. Therefore, the dispersion angle ($\delta\theta$) assumed by the ST method is
1339 overestimated in our 2D simulations, where fast magnetosonic modes determine the evolution
1340 of the magnetic field and striations, which are extremely well-aligned. This leads to signifi-
1341 cantly underestimated magnetic field strengths compared to the true value. However, due to
1342 the presence of Alfvén disturbances, the DCF method is still able to match the true magnetic
1343 field strengths from our 2D simulations, at least up to medium magnetic fields. For stronger
1344 magnetic field strengths, DCF methods also overestimate the dispersion angles, as they only
1345 consider the effects of Alfvén disturbances, which, after certain evolutionary timescales, are
1346 not significant compared to the magnetic pressure created by magnetosonic modes, causing
1347 dispersion in the magnetic fields (mainly the B_y component) to decrease, and underestimations
1348 of magnetic field strengths. In these regions, we expect an improved methodology that can take
1349 into account the compressive effects that form and derive striations.